

# Optimisation of a Near-Field Scanning System

*Presented by*

**Enda McLoughlin, B.Sc. (Hons.)**

A thesis submitted for the degree of

**Master of Science**



**NUI MAYNOOTH**

Ollscoil na hÉireann Má Nuad

*Terahertz Optics Group*

Department of Experimental Physics

NUI Maynooth, Maynooth

Co.Kildare, Ireland

**3rd July 2012**

*Head of Department*

Prof. J. A. Murphy , M.Sc., M.S, Ph.D.

*Research Supervisor*

Dr. Marcin Lukasz Gradziel, M.Sc, Ph.D.

# Contents

<b>1</b>	<b>Background</b>	<b>8</b>
1.1	Astronomical Applications . . . . .	9
1.2	Other Applications . . . . .	14
1.3	Purpose of Work . . . . .	19
<b>2</b>	<b>Existing System</b>	<b>21</b>
2.1	Network Analysis . . . . .	23
2.1.1	Principles of Network Analysis . . . . .	24
2.1.2	ZVA-24 and ZVA-Z110 . . . . .	27
2.2	XY Scanner . . . . .	30
2.2.1	XY Scanner Configuration . . . . .	31
2.2.2	Stepper Motors and Driver Boards . . . . .	32
2.2.3	Other Components . . . . .	34
2.3	Measurement Method . . . . .	35
2.4	Improving the Scanning System . . . . .	37
<b>3</b>	<b>System Upgrades and Vibration Analysis</b>	<b>38</b>
3.1	System Upgrades . . . . .	39
3.1.1	Motion Control Upgrade . . . . .	40
3.1.2	Additional Translation Stages . . . . .	43
3.1.3	New Safety Features . . . . .	45

3.1.4	Problems due to the Upgrade . . . . .	46
3.2	Analysis of Converter Head Displacement . . . . .	49
3.2.1	Calibration of Accelerometer . . . . .	51
3.2.2	Position Profile Extraction . . . . .	52
3.2.3	Conclusions, Problems and Possible Solutions . . . . .	54
3.3	Spectral Analysis of Vibration . . . . .	55
3.3.1	Analysis of Original Data Set . . . . .	57
3.3.2	Motion Improvement and Further Analysis . . . . .	60
3.3.3	Structure of Excitations . . . . .	62
3.4	Results and Conclusions . . . . .	65
<b>4</b>	<b>Development of Beam Alignment Technique</b>	<b>67</b>
4.1	Current Methods . . . . .	68
4.2	New Method . . . . .	69
4.2.1	Model Construction . . . . .	71
4.2.2	Gaussian Beam Model Summary . . . . .	76
4.2.3	Complex Levenberg-Marquardt Implementation . . . . .	77
4.2.4	Initial Guesses for LM Fitting . . . . .	80
4.2.5	Testing the Fitting Method . . . . .	85
4.2.6	Fitting Measurement Data . . . . .	88
<b>5</b>	<b>Conclusions</b>	<b>93</b>
5.0.7	Possible Future Work . . . . .	95

# Acknowledgements

I really believed that this would be, by far, the most straightforward part of my thesis to write, but alas the scientific method again disproves one of my theories. Throughout the time that I spent writing the main body of work I looked forward with great anticipation to this moment, a time when I could sit down and thank all of the people who have supported me on my academic journey. However, after an embarrassing amount of attempts I have decided that this draft of the acknowledgements will be the final draft.

To begin by breaking the mould, I would first like to offer an apology rather than thanks to anyone that I forget to mention by name in the following lines. I do like to believe that everyone who has been part of my life, during my miniature lifetime in University, already knows how important they are to me.

The ones most deserving of thanks are my family, especially my parents. To Mum and Dad I would like to simply say, thank you for always being there and for always understanding. Your support is as much a Universal constant as Planck's and I hope that I will be able to repay this in kind. The same goes for my siblings and their respective spouses; Benny and Nat, Adrian, Lou and Dec and Michéal, among everything else cheers for the free dinners and not holding it against me when my round always seemed to coincide with the train home...

As far as academic support goes, I must give my sincerest thanks to my supervisor Dr. Marcin Gradziel. I don't know how I will ever be able to express my gratitude for the patience you've showed me over the last few years. From the very first days of building the scanner in 2008 to the preparation of my thesis seminar you've taught me so much, thank you.

To the other staff members that make up the THz research group I would also like to express my gratitude. Prof. Murphy, Dr. O'Sullivan and Dr. Trappe, your doors were always open and I don't remember a single occasion when I wasn't greeted with a smile, thank you for everything.

My time in Maynooth as a post grad gave me a fantastic opportunity to develop my teaching skills. I adored working in the labs for Dr. Peter van der Burgt, Dr. Michael Cawley and Dr. Frank Mulligan. Thank you all so much for the fantastic experience and feedback over the years, some of my best memories of college are from those labs. I would also like to thank Gerard McMahon for helping me prepare for my first lecture course. A special thanks also goes to Dr. Niall McKeith, who not only was a great help throughout my time teaching in the first year labs but also gave me the opportunity to take care of the National Science Museum during the Summer. Another special thanks goes to Tully Peacocke, who not only was a great help with my own research but also took the time to help me prepare for an interview in my final year, thank you.

To the departmental secretary, Grainné Roche, no words will do justice to my appreciation of the job that you do in the department. I always enjoyed our chats and will consider you one of the best friends that I made in Maynooth.

To John, Pat, Marie, Dave W, Ian and Derek I want to say how I honestly believe that you make up the best technical staff in the University. To add to the help

every single one of you were to me over the year I would also like to say how much I enjoyed getting to know all of you. Thank you for giving me the chance.

A special word for fellow post-grad Dan W, you have no idea how delighted I was when I heard you were coming back to do research. It was great to have a friend, housemate and colleague that I knew so well from my time as an undergraduate.

To all those that put up with my incessant nattering while sharing an office with me, you have the patience of saints. This means you Dave B, Ronan H, Stephen, Darragh and Paul McL. It would not have been the same without you guys. To Dean, I want to say how great it was to be starting my research with a familiar face. Thank you for always being the same great guy.

Donnacha, the nocturnal hours that you kept always had me expecting to see you hanging from the ceiling by your feet when I went to your office. Brian, even though you spell your name incorrectly you're still good in my books. Mairead, I expect you to be wearing your MicroWave Wizards hat on graduation. Ronan, I'm thinking about trying to beat the eggheads if you were up for it. To all of you, thanks for making my time in Maynooth just that bit more enjoyable, you're all fantastic.

Francis, Bertie, Colm, Andrew, Stephen and Paul, more names that, for me, represent some of the most friendly people I've had the pleasure of working with. I'm sure our paths will cross again in the future.

At this point I believe I've gone on for long enough. I was going to write a list of names of others that have made my time in Maynooth so much better in so many ways but instead I'm going to say a big thank you to Maximus for feeding me, O'Neills for sheltering me and I think everyone else already knows how I feel.

## Abstract

In this thesis, the optimisation of a near field scanning system is discussed. This system, which consists of a stationary transmitter and a movable receiver, is in use in the Experimental Physics Department at NUI Maynooth. The position of the receiver is controlled by a two axis mechanical actuator.

The function of the near field scanning system is to characterise and verify different optical components in the W-Band (75 – 110 GHz). The measurements are generally used as a comparison with optical set-ups that have been modelled in commercial optical packages such as CST, GRASP and ZEEMAX.

Primarily this project is concerned with improving the overall efficiency of the scanning system. At first the original set-up will be introduced along with the reasoning behind subsequent upgrades. In Chapter 3 these upgrades to the system will be outlined along with the problems that arose as a result. In particular, a study of the mechanical vibration caused by the driving of the actuator is discussed. This vibrational study is split into two parts; displacement analysis and spectral analysis. Both methods are used in an attempt to understand the source of these new excitations. The implications that these vibrations have on the quality of measurements being made by the near field scanner will also be outlined.

Finally, the development of a new computational tool for alignment will be discussed. The purpose behind this work is to develop a robust alignment tool that will be the centrepiece of a standardised alignment method. The construction of this tool along with its step by step testing will be outlined in Chapter 4.

# 1 Background

The work presented in this thesis was carried out as part of the Terahertz Research group at NUI Maynooth. The research group is predominantly interested in the development of optical systems for space and ground-based astronomical instruments in the mm and sub-mm range. This involves not only the modelling of optical systems but also the testing and verification of individual components. Terahertz research, as a field, is quite new but is becoming more and more active as it is probably the least understood part of the electromagnetic spectrum.

Until recently, the sources and detectors being used in the THz range were quite cumbersome and expensive. Originally free electron lasers (FELs) were generally used to generate THz radiation. The output of these devices is generated by the interaction of a beam of relativistic electrons and an oscillating magnetic field which can be tuned to change the wavelength of outputted radiation. Passively-cooled bolometers would have been the most commonly used detectors when the field was in its infancy. These detectors had very poor noise performance and their actively cooled counterparts were costly to run as a supply of liquid helium is required in order to keep them at their operating temperatures. The lack of relatively cheap, efficient and reliable sources and detectors therefore caused this region to be dubbed the "Terahertz Gap".



The "Terahertz Gap" itself covers a bandwidth of .03 mm to 3 mm, sandwiched between the far-infrared and microwave regions of the electromagnetic spectrum. For the purposes of testing components sub-millimeter radiation would generally be transmitted as a free space beam through an optical system. Unfortunately the majority of components in use are comparable in size to the wavelength of radiation and diffraction becomes an issue. Due to this, techniques which could normally be used for propagation analysis of a beam (physical optics, ray tracing) become less accurate and far less efficient. A technique known as Gaussian Beam Mode Analysis (GBMA) can be used to solve some of these problems and model these "quasi-optical" systems [1].

In this chapter I will briefly describe the main driver for advances in the Terahertz field, namely astronomical observations of the Cosmic Microwave Background (CMB) with the aim of quantifying its temperature anisotropies. Without the advances in sources and detectors (resulting from work in astronomy), we would not be seeing the advent of new terahertz technology for applications in fields such as medical imaging, security scanning and quality control.

## 1.1 Astronomical Applications

The advances in the field of terahertz radiation have been motivated by a need to develop terahertz detectors for astronomical observations. It is certain that some of the most important measurements being made today in the area of cosmology are those of fluctuations in the CMB. These measurements of the fluctuations are being taken to a new level with the ESA Planck surveyor [2] which is equipped with detectors in the sub-mm range. The CMB is relic radiation left over since the cataclysmic event known as the Big Bang (believed to have occurred around 13.7 billion years ago). It has been studied closely since it was first accidentally

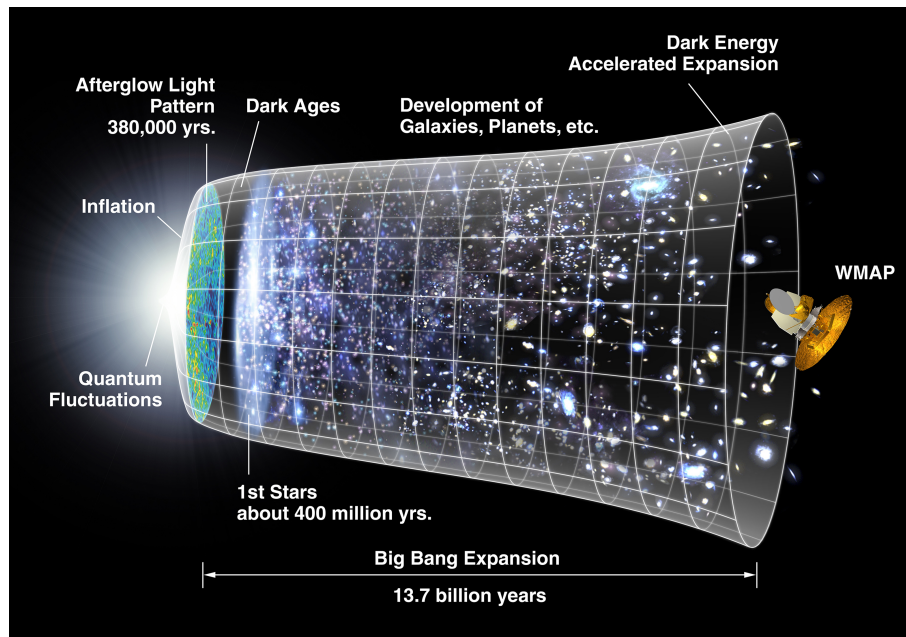


**Figure 1.1:** An illustration that was used to show the purpose of the WMAP mission. The CMB is a snapshot of the "Surface of Last Scattering" the earliest point at which we can observe the Universe [4]

detected by Robert Wilson and Arno Penzias using a Dicke radiometer at Bell Laboratories in 1965 [3].

The Big Bang is the event from which it is believed the Universe spawned and an illustration of this process is shown in figure 1.1. It is an explosion of infinitely dense space causing the creation of subatomic particles and therefore matter. The remnant radiation that is observable today decoupled from matter about 380,000 years after the Big Bang and is the earliest era in the lifetime of the Universe that we can observe. Prior to this, the universe was a hot, dense plasma of photons, electrons and protons making the universe opaque to radiation [5].

Original measurements of the CMB indicated that there was a uniform background temperature of the universe; however this does not make sense. If the background radiation is uniform in all directions then why is the universe itself

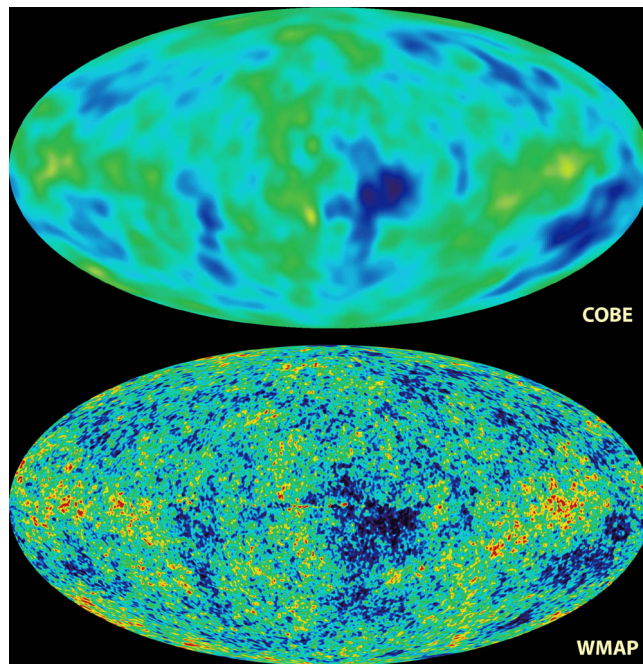


**Figure 1.2:** NASA's COBE satellite measured the CMB from space and detected fluctuations in the background temperature. WMAP was COBE's more sensitive successor [6] [7].

not a uniform distribution of matter? For this reason it was predicted that there would have to be anisotropies in the CMB in order to give us the large scale structure we see in the Universe today. To detect these temperature fluctuations much more sensitive measurements would have to be made [5].

NASA's COsmic Background Explorer (COBE) satellite was the first space-based mission to detect fluctuations in the CMB. These measurements were then improved on by its successor, the Wilkinson Microwave Anisotropy Probe (WMAP) which had much greater sensitivity. Figure 1.2 shows a comparison between the sensitivity of measurements using COBE and WMAP [6] [7]. A huge effort has been put into the development of more sensitive sub-mm detectors for astronomy for both ground-based and space-borne missions to measure the background radiation (Planck Surveyor, QUaD, ALMA).

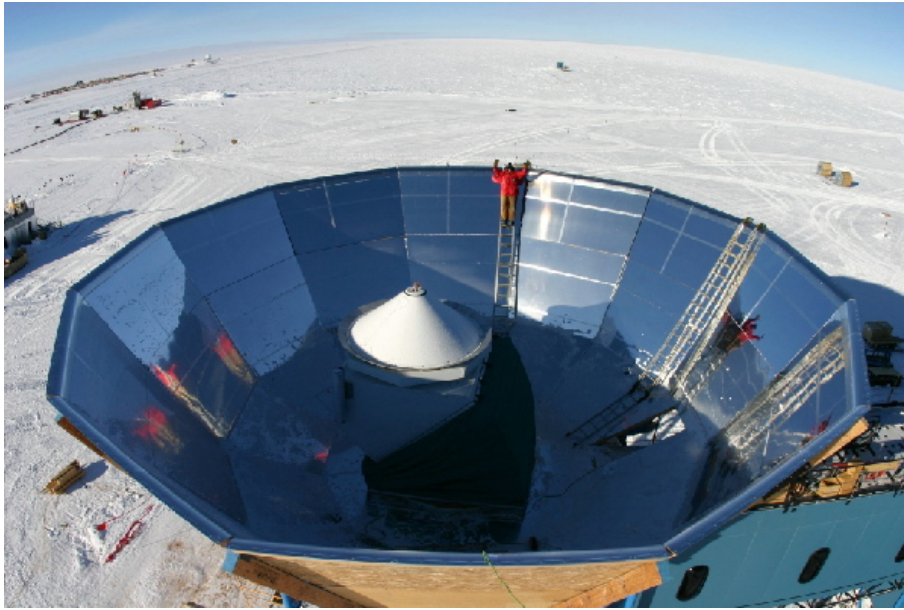


**Figure 1.3:** The QUEST (Q and U Extragalactic Sub-mm Telescope) instrument which is used for studying the polarisation of the CMB. The instrument is located in Antarctica and is described as QUEST at DASI (QUaD) [8].

QUaD is a ground-based mission that involved the replacement of the DASI interferometric array with QUEST (a bolometric detector). A ground-based mission, like QUaD, suffers its biggest challenge in overcoming the absorption of THz radiation by the water vapour content in the atmosphere. QUaD is located at the driest place on Earth, Antarctica. The dryness of the atmosphere results in much less attenuation of THz radiation than at other sites on the planet. Figure 1.3 shows an image of the QUEST instrument where it is housed in the original DASI mechanical infrastructure [8].

The ESA Planck surveyor was launched in May 2009, and its goal is to create a detailed map of the CMB with sensitivities surpassing that of its predecessors [2]. The satellite along with the ESA Herschel mission is orbiting around the second Lagrange point in the Earth-Sun system. The L2 point is located outside the Earth's umbra and therefore is not totally eclipsed from the Sun but there it

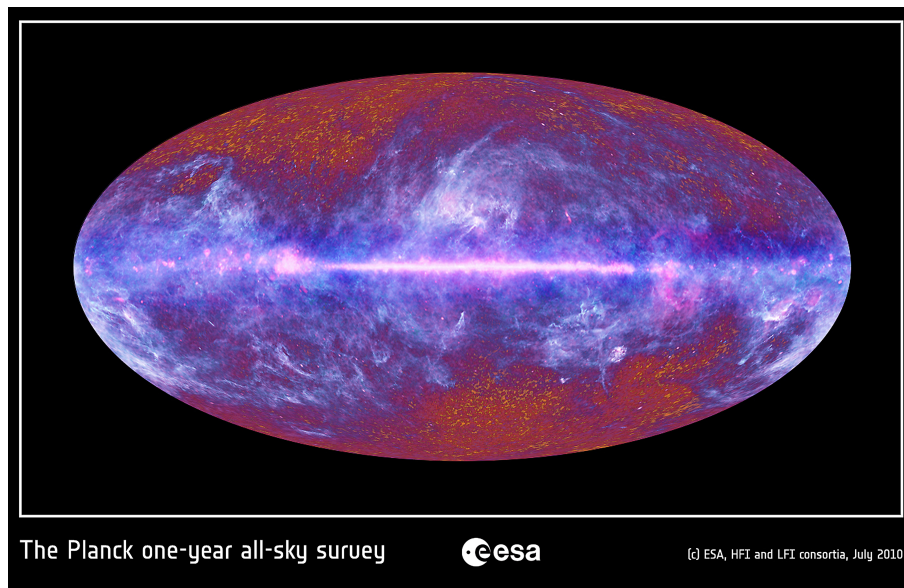


**Figure 1.4:** This is an image of the unprocessed data from the ESA Planck surveyor. The image is dominated by cold dust regions in the main disc of our galaxy [9].

is still advantageous as the satellite stays in the same orientation in the Earth-Sun system. This allows for the sensitive detectors, which need to be cooled, to be shielded properly. This feature is very important for measurements as Planck's detectors operate at less than 100 mK.

The initial year long full-sky survey performed by Planck has already been completed and the images were released to the public in the summer of 2010 (figure 1.4 shows this public release). These images however are dominated by the main disc of our galaxy, showing the cold dust regions that are areas of star formation. A large amount of post-processing must be performed on these images in order to remove the foreground and leave just the image of the CMB. It is hoped that these more accurate measurements of both the temperature and polarisation of the anisotropies in the CMB will lead to the clarification of theories on the origin of the universe.



**Figure 1.5:** The Atacama Large Millimeter/sub-millimeter Array is an interferometric array of 66 telescopes. The site is due to be fully operational by the end of 2012 [10].

The Atacama Large Millimeter Array (ALMA) is a ground based mission also working in the mm and sub-mm range. Unlike the two previous examples, ALMA is not concerned with the CMB. Instead, the main goal of the project is to study the birth of stars in the early universe. Along with this it should provide detailed images of nearby cold dust regions of star and planet formation. The array consists of 66 separate telescopes that are used as a large interferometer [11]. As the individual telescopes can be moved on tracks the baseline can be adjusted and this allows for a variable zoom. An image of the array which is due to be fully operational by the end of 2012 can be seen in figure 1.5.

## 1.2 Other Applications

One of the main constraints on technological development in THz physics was the lack of good THz sources and the cost of those that were available. As is generally the case the development of technology for scientific research has lead to the

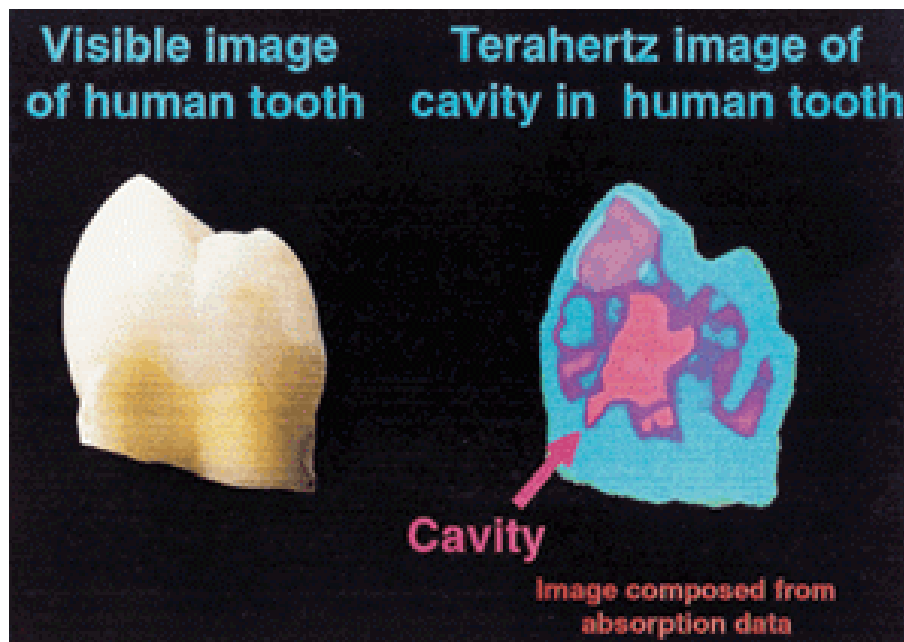


**Figure 1.6:** An image of a human tooth composed from terahertz absorption data. Here a cavity in the tooth can be clearly seen. This image represents work carried out by TREL in Cambridge [12].

development and improvement in many other fields. The advent of solid-state THz detectors that are capable of operating at room temperature is certainly proving this.

One such field that has exciting possibilities is that of medical imaging. Terahertz radiation offers higher resolution than microwave, and is non-ionising. This makes terahertz very useful for imaging techniques used on the human body. Tissue is not damaged by its interaction with terahertz radiation as is the case in more conventional scans that use x-rays. Figure 1.6 shows an application of terahertz imaging in dentistry.

Water is an absorber of THz and for astronomical purposes this is a large disadvantage, especially for ground observations. However, the attenuation of THz due to absorption in water actually has both advantages and disadvantages for medical imaging. Figure 1.7 shows how a difference in water content can be

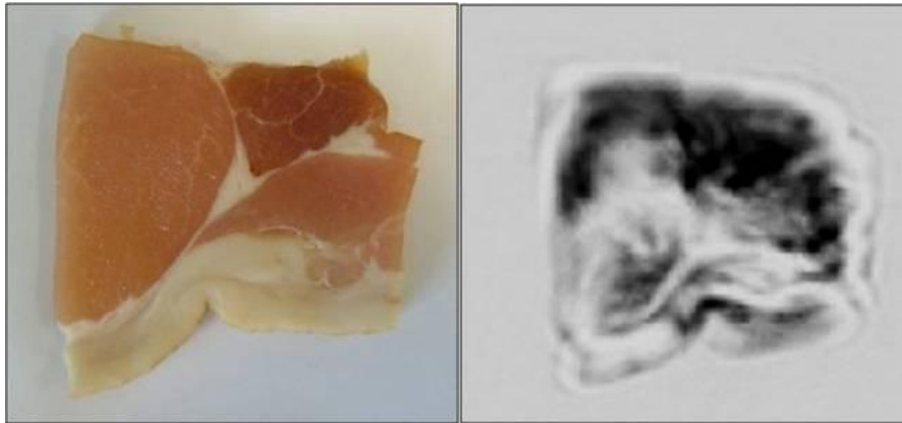


**Figure 1.7:** An example of how water content effects the absorption of THz radiation from the work of Ian McAuley and Leanne Young at NUI Maynooth. [13].

imaged using THz radiation. The image on the right of figure 1.7 has been constructed from the reflection of a beam incident on a slice of bacon. Areas of fatty tissue contain more water than the lean tissue and therefore have a different level of absorption. The bright and dark areas in the right image correspond to the areas of fat in the picture on the left [13].

During a process like the healing of a wound, there is a change in the amount of water surrounding the healing tissue. By studying this water build-up the healing of a wound can be investigated. This method combined with the fact that fabrics are transparent to THz radiation would allow for the monitoring of the healing process without ever removing a dressing. Deposits of water also gather around cancerous cells, meaning that there might be applications for THz in the early detection of skin cancer. Unfortunately the attenuation of THz by water also restricts the penetration depth of medical scans in much the same way as it restricts where we can perform ground-based astronomy.

Security applications for THz are being heavily investigated with some airports currently using full body THz scanners on a trial basis (fig. 1.8). These scanners are being used to detect metallic weaponry under clothing through the reflection



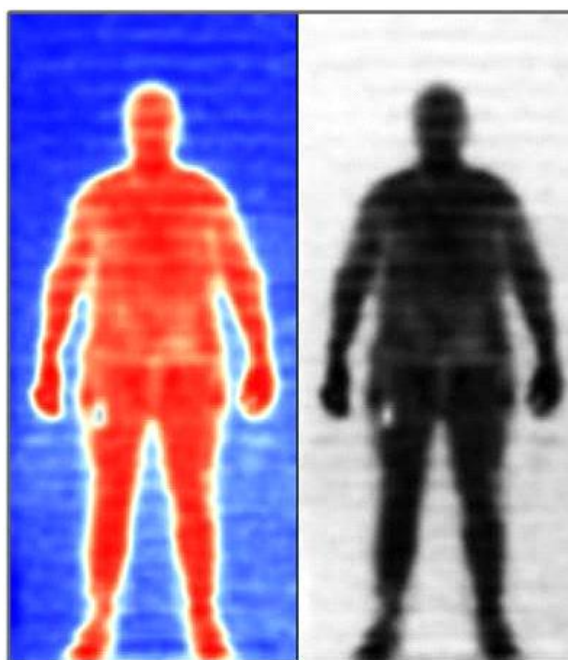


**Figure 1.8:** An example of the passive security imaging being trialed in airports. This image was taken using the T8000, a passive THz scanner developed commercially by Thruvision Systems of Oxford [15].

of THz radiation. Similar methods are also being tested for the remote detection of concealed explosives and narcotics. This is possible as many materials of interest have unique spectral "fingerprints" in the terahertz range which allows for a combination of both imaging and spectral identification [14].

There are also applications for THz imaging in field of quality control. Pharmaceutical companies have seen the possibilities of using THz pulsed spectroscopy and imaging, to study the crystalline structure of molecules and the integrity of tablets.

A prominent issue in the development of new pharmaceuticals is the presence of polymorphs. Polymorphism is defined as the ability for a solid material to exist in more than one crystalline structure. It is important to be able to identify these different structures as drug patents usually only cover one arrangement of the

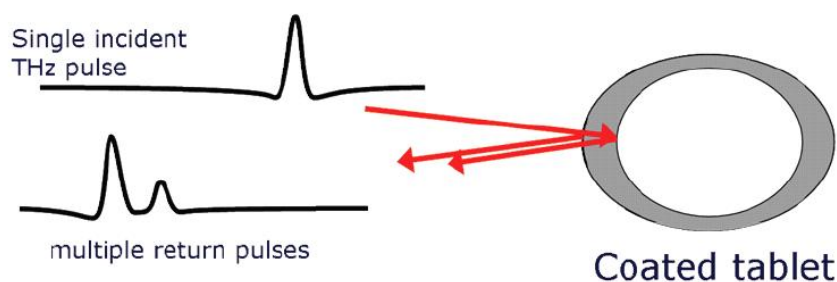


**Figure 1.9:** The process of determining tablet coating thickness and integrity is illustrated here. By studying the delay between reflected pulses the thickness of the coating can be determined [17].

crystal. The quality control aspect of this is the change in solubility of a crystal depending on the polymorph i.e. one structure may be more therapeutically active than another of the same molecule. For these reasons the identification of the different polymorphs through methods of THz pulsed spectroscopy may become a very useful technique [16].

The main quality control application of THz pulsed imaging (TPI) is the measurement of tablet coating thickness and integrity (Figure 1.9). The coatings on tablets are not just for aesthetic purposes; one of their main functions is the control of the dosing rate of a particular drug. In cases where the integrity of the coating is damaged, the dosage rate may be skewed. Dose-dumping is the extreme case of this which can be life threatening. As a result there are both legal and commercial implications which require accurate understanding of coating quality [17]. There is a reflection every time THz radiation passes from one material to another. By looking at the separation between these reflections and knowing the refractive index of the material the thickness of each region can be calculated. Work is currently being carried out on this particular area at Cambridge University in conjunction with TeraView [17].

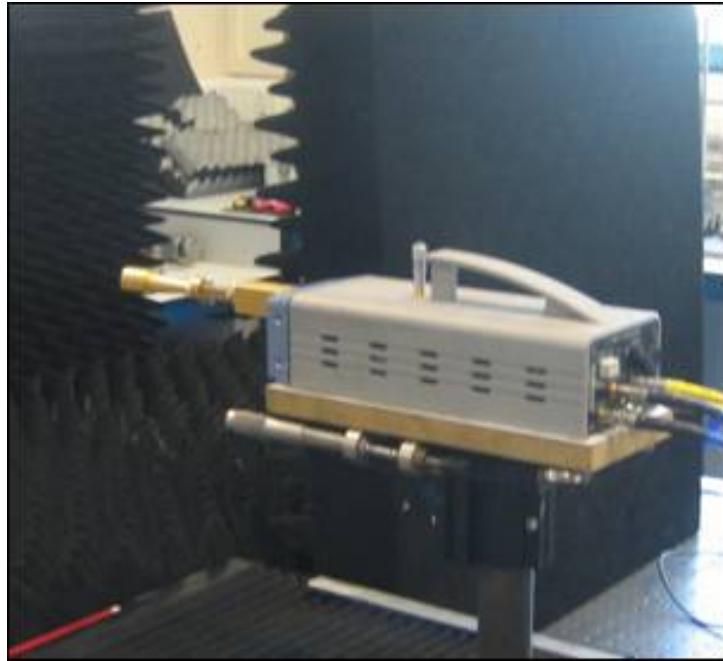


**Figure 1.10:** A W-Band frequency converter heads being used in conjunction with a VNA. This converter extends the operational bandwidth into the W-Band by mixing a stimulus signal with a local oscillator.

### 1.3 Purpose of Work

It can be seen from the wide variety of applications presented so far that there is a real scientific and technological impetus for research in the field of THz radiation. Understanding not only how THz radiation propagates, but how the optical components used in quasi-optical systems interact with the radiation is very important.

The THz laboratory in the Experimental Physics Department at NUI Maynooth is dedicated to the testing and performance verification of quasi-optical components and the characterisation of simple quasi-optical systems. Measurements are made using a near-field scanner which utilises a Rohde and Schwarz Vector Network Analyser (VNA) and two W-Band converter heads. One of these converter heads is pictured in 1.10. This set-up allows for the transmission and reception

of radiation in the 75 – 110 GHz range.

The biggest advantage of the VNA is that it allows for the measurement of both the amplitude and phase of the radiation being propagated. Single-point measurements do not give enough information about the field after it has propagated through a quasi-optical system, especially if we are interested in the diffraction effects of particular components. For this reason, it is necessary for at least one of the converter heads to be dynamic in order for us to build a two dimensional image of the surface of the beam.

Alignment of the two converter heads is very important for the types of measurements we perform. In order to improve the system a new alignment procedure was developed and this will be outlined later in the thesis. In fact all of the work that will be presented here concerns improvements not only to the quality of the measurements using the near-field scanner but also the efficiency of scanner system itself. It is my hope that the work from this project will allow further confidence in any future measurements performed using the scanning system. However, we must first start with detailing the existing system and the subsequent mechanical and electronic upgrades.

## 2 Existing System

The particular measurements that will be discussed in this thesis involve the propagation of THz radiation through either an optical system or free space. For the purpose of transmission, horn antennae are used to facilitate the transition of the radiation into free space. These quasioptical components also ensure a smooth Gaussian distribution of the beam. Due to diffraction effects, the beam spreads out transversely to the axis of propagation as it travels from transmitter to receiver.

In order to characterise the transmitting horn, or any other optical component, it is necessary to measure the amplitude of the beam. However, as the beam undergoes diffraction the movement of the receiver in order to encompass the entire beam must be facilitated. A two dimensional actuator system is used to allow the receiver position to be dynamic. This scanning system allows for the adjustment of the receivers position in a plane that is typically perpendicular to the axis of propagation. This plane is defined by the horizontal x-axis and vertical y-axis, while our beam is said to propagate along the z-axis. A schematic of the scanning system can be seen in figure 2.1.

The determination of the amplitude of the propagating beam is performed by a Rohde and Schwarz ZVA-24 Vector Network Analyser (VNA). The VNA is used in conjunction with two W-band (75 GHz to 110 GHz) frequency converter

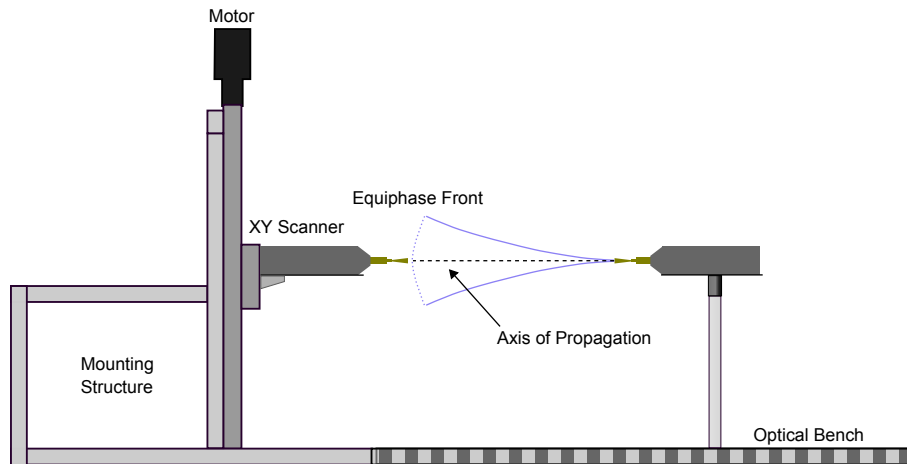


**Figure 2.1:** The radiation emanating from the horn antenna spreads out rapidly as the beam propagates. In order for a measurement to encompass the entire beam the receiving head must be moved to different positions using the XY scanner.

heads [20]. Both converter heads are operated simultaneously by the VNA. One is treated as the transmitting port and the other as the receiving port. The VNA allows us to measure the complex amplitude of the transmitted signal which means that the phase of the electric field can be recovered as well as the magnitude. This is made possible through the comparison of the received signal with the stimulus that was originally used to create it.

For measurements involving the propagation of a beam through free space the receiving converter head is mounted on the XY scanner. This allows for the measurement of the complex amplitude of the electric field at multiple points on a planar surface. During this process the position of the transmitting head is usually kept static. There are, however, occasions when it is useful to mount the transmitter on a separate translation stage for the adjustment of the propagation distance. This is usually the case for measurements where we are interested in any standing waves that may be set up between the two ports.

The measurements described are used to verify many different types of optical

components such as horn antennae, lenses, gratings, waveguides and cavities at multiple frequencies in the 75 GHz to 110 GHz range. The results are then used to not only investigate the performance of particular components at different frequencies, but also to verify the accuracy of models built in commercial software packages such as CST, GRASP, ZEMAX and Microwave Wizard. Measurements have also been used to verify results from software packages that have been developed in the Experimental Physics Department at NUI Maynooth e.g. MODAL and SCATTER.

In most cases, the measurement data is handled by a software package called GHOST. This software was developed in the LabVIEW environment at NUI Maynooth by Dr. Marcin Gradziel and is currently at version 2. The VNA itself is connected, via GPIB, to another computer that has the GHOST software installed on it. This computer is used for the storage of the measurement data along with being responsible for the driving of the scanning system. As well as handling data from the VNA, GHOST also has the ability to collect data from other analog devices such as a 3-axis accelerometer. This device, which is used for vibrational analysis, will be discussed in detail in Chapter 3.

## 2.1 Network Analysis

The measurements being performed in the Terahertz Optics Laboratory are made possible through the use of a ZVA-24 Rohde and Schwarz Vector Network Analyser. The VNA is designed to operate from 10 MHz as far as 24 GHz. With the addition of two ZVA-Z110 converter heads the operating frequency can be stepped up to the W-Band (75 GHz to 110 GHz).

As mentioned, at the beginning of this chapter, the VNA allows us to not only



**Figure 2.2:** The Rohde and Schwarz ZVA-24 vector network analyser in use at the Experimental Physics Department, NUI Maynooth. This model of network analyser is constructed using the heterodyne approach and contains multiple oscillators.

measure the magnitude of an electric field but also its phase. Knowing the phase profile of a propagating beam, gives us a large amount of information on factors like propagation distance and radius of curvature. This extra information is invaluable for the alignment techniques developed and discussed in Chapter 4.

### 2.1.1 Principles of Network Analysis

Network Analysis is a technique commonly used in RF engineering for the analysis of electrical circuits. The technique involves the measurement of the network parameters of a device under test (DUT). There are different types of network parameters that can be measured, for example, admittance parameters ( $A$ -parameters) and impedance parameters ( $Z$ -parameters). However in most modern Network Analysers, the network parameters that are commonly measured are the  $S$ -parameters. Measurement of reflection and transmission at higher frequencies is relatively simple and it is for this reason that the scattering para-



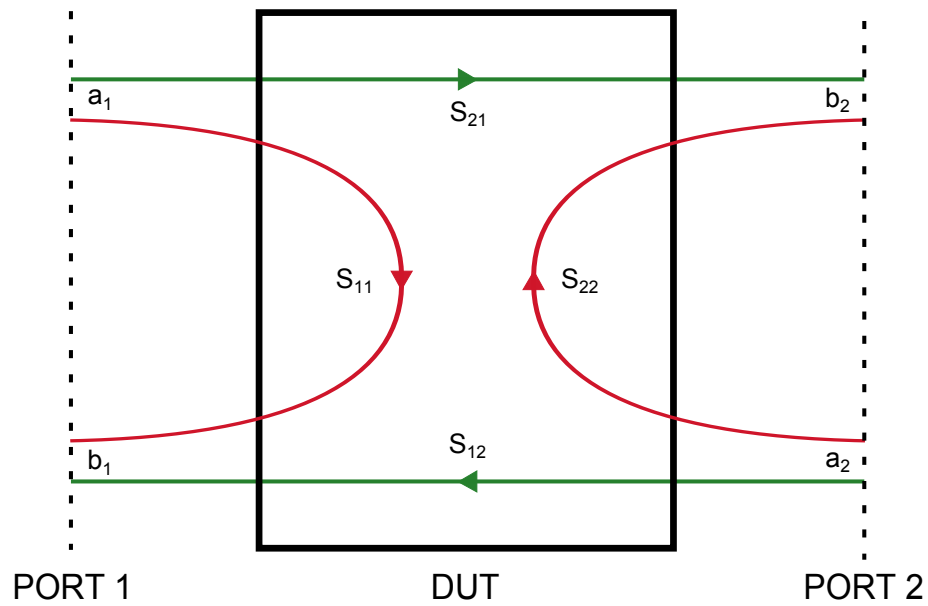


**Figure 2.3:** An example of a two port system and the scattering parameters of a device under test. Ports 1 and 2 both have incident and reflected waves, 'a' and 'b' which are dependant on the scattering parameters.

parameters are preferred [18]. The amount of  $S$ -parameters that can be measured is dependent on the number of ports involved in the network. If there are  $N$  ports in a network then it is possible to measure  $N^N$   $S$ -parameters.

In figure 2.3 an example of a simple two-port network can be seen. The incident and reflected waves from each port are shown and it can be seen that the waves entering each port are linked by the scattering parameters of the device under test (DUT). The relationship between the reflected waves and the incident waves is outlined in equations 2.1 and 2.2

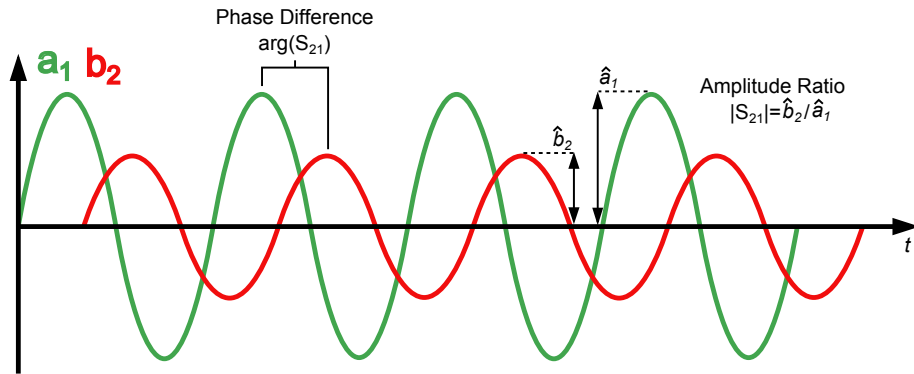


**Figure 2.4:** Shown is an example of the sinusoidal test signal that is generated by the network analyser;  $a_1$  is the incident wave from port 1 and  $b_2$  is the response at port 2.

$$b_1 = a_1 S_{11} + a_2 S_{12} \quad (2.1)$$

$$b_2 = a_2 S_{22} + a_1 S_{21} \quad (2.2)$$

It is more common to write these two equations as the scattering matrix  $S$ . This matrix is shown below in equation 2.3

$$\begin{bmatrix} b_1 \\ b_2 \end{bmatrix} = \begin{bmatrix} S_{11} & S_{12} \\ S_{21} & S_{22} \end{bmatrix} \begin{bmatrix} a_1 \\ a_2 \end{bmatrix} \quad (2.3)$$

All network analysers generate a sinusoidal test signal that is applied to the DUT. This test signal is known as the stimulus and is used as a reference when looking at the response of the DUT. This response will also be sinusoidal but will generally have a different value for both phase and amplitude as shown in figure 2.4.

At this point it is necessary to note that there are two main categories of network analyser, namely the scalar network analyser (SNA) and the vector network analyser (VNA). SNAs only measure the amplitude difference between the stimulus and response wave quantities, whereas VNAs also measure the phase difference

[19]. Vector network analysers like the one in use here at NUI Maynooth require a much more complex implementation than their scalar counterparts.

Much like the two categories of network analysers, there are also two categories of vector network analysers. They may be constructed using either a homodyne or heterodyne approach. The homodyne approach to VNA construction involves just a single oscillator which is used to provide both the stimulus and process the response. These analysers are relatively economical but have many technical limitations when compared with the more robust heterodyne VNAs [19]. From this point on we will only consider the heterodyne approach to vector network analysis.

### 2.1.2 ZVA-24 and ZVA-Z110

The Rohde and Schwarz ZVA-24 is a VNA constructed using the heterodyne approach. Without the use of the frequency extension capabilities of the W-band converter heads, the VNA operates in the frequency range of 10 MHz to 24 GHz.

The VNA itself is split into four main stages: the generator, the test set, the receivers and the computer. The generator provides the RF signal for each of the test-ports, this signal is known as the stimulus. The source switch present in the generator is used to select which port the stimulus is sent to and at this point the selected port is operated as an active test port.

The test set in figure 2.5 is a set of two test ports. As the stimulus enters a port it first passes through an attenuator. This device is used to control the total output power of the test port. The signal is then passed through a splitter resulting in two identical waves, one of which is sent to the reference channel while the other

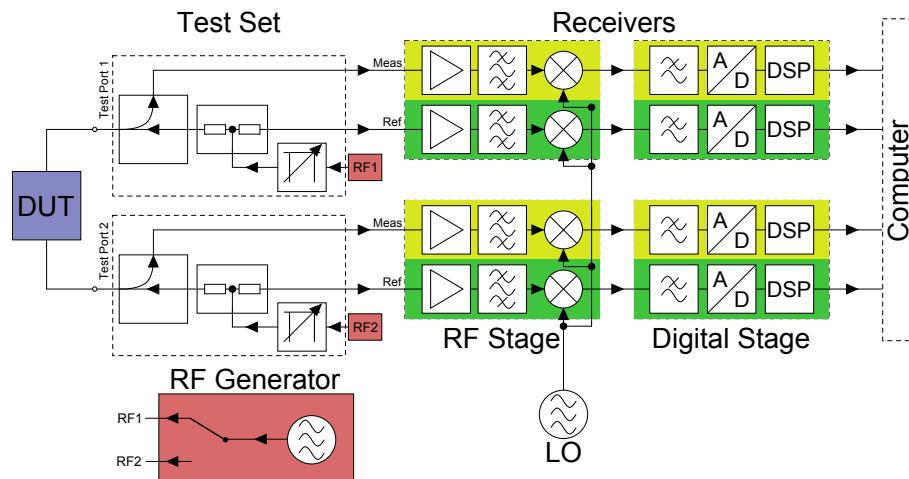


**Figure 2.5:** A 2-port heterodyne vector network analyser. The generator is used to create the stimulus for the test set. The measurement and reference receivers are then fed by the test set and the resulting information is digitised.

is sent to the device under test (DUT). The test port also receives the reflected wave returning from the DUT and sends it to the measurement channel. In essence, the test port has now split up both the incident and reflected waves and sent them to separate channels.

The measurement and reference channels are split into two different receiver stages. The first stage combines the two incoming waves with a local oscillator that is separate from the stimulus signal. Once the waves have been mixed down to a suitable frequency they pass through the second stage of the receivers. This is a digital signal processing stage and converts our RF signals into complex numerical values that are to be passed to the computer. At this point in the processing chain the error correction values ascertained from the calibration of the system are applied to the data. For a two port system the standard calibration procedure is called TOSM (Thru-Open-Short-Match). For the most part this involves the use of a standardised calibration kit that contains optical components with known responses. However, for a measurement like "Thru"

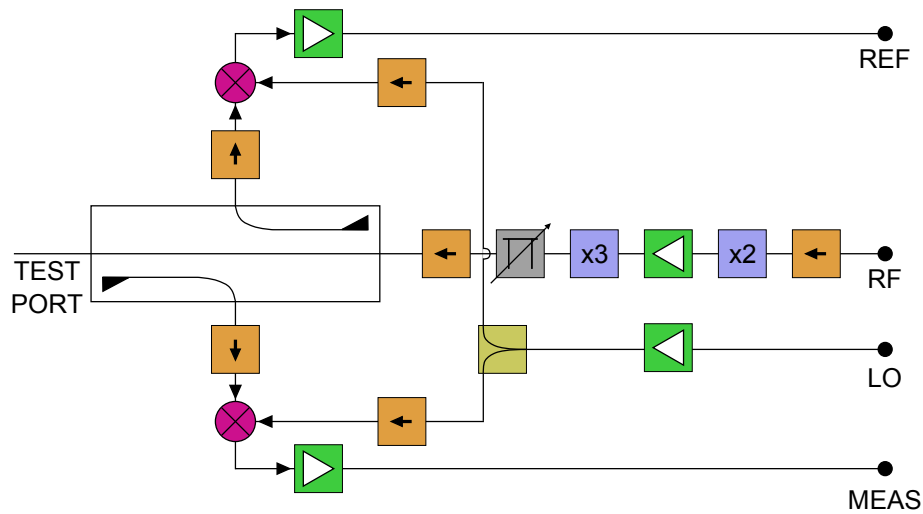


**Figure 2.6:** A block diagram of one of the two ZVA-Z110 frequency extension heads in use. These modules extend the range of the VNA into the W-Band (75 GHz to 110 GHz).

the two ports just need to be connected directly to each other allowing for what should be perfect transmission. A measurement like this allows for reflections inside the ports to be calibrated out of the data.

In order to change the operational band of the VNA to the W-band (75 GHz to 110 GHz), the system incorporates two ZVA-Z110 frequency extension heads. A block diagram of one of these frequency extension heads is shown in figure 2.6. Each uses two of the test ports from the ZVA-24, one port for the stimulus and the other for local oscillator and are connected as in figure 2.7. The stimulus is split inside the converter head into two identical signals, one is outputted to the DUT while the other is sent back to the reference channel. The input to the head is directed to the measurement channel. Both of the signals being sent to the VNA are mixed down using the same LO and enter the measurement and reference channels of the test port responsible for the stimulus.

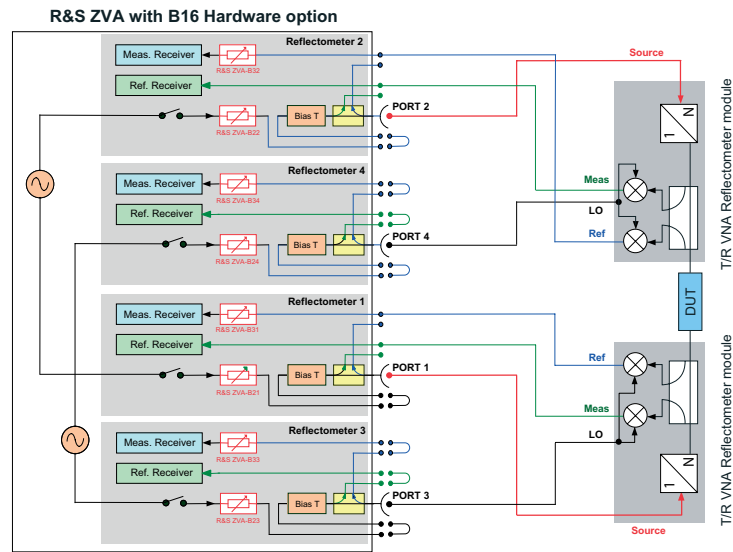


**Figure 2.7:** This block diagram shows how the two ZVA-Z110 frequency extension heads are connected to the ZVA-24. The multiple internal signal generators of the ZVA-24 provide the stimulus and LO frequencies for both heads simultaneously [20].

## 2.2 XY Scanner

Both ZVA-Z110 frequency extension heads can act simultaneously as transmitter and receiver. For studying how a beam is transmitted from an antenna, one of the heads is considered to be the transmitter and kept stationary while the other is mounted on an XY scanner and treated as the receiver. This mounting allows for the changing of the position of the receiver with respect to the transmitter. With a dynamic receiver we can construct a grid of data points and recover an image of the beam's complex surface.

The XY scanner consists of two screw actuators driven by stepper motors. These are devices that allow for the accurate movement of a central piece of iron through multiple discrete positions.

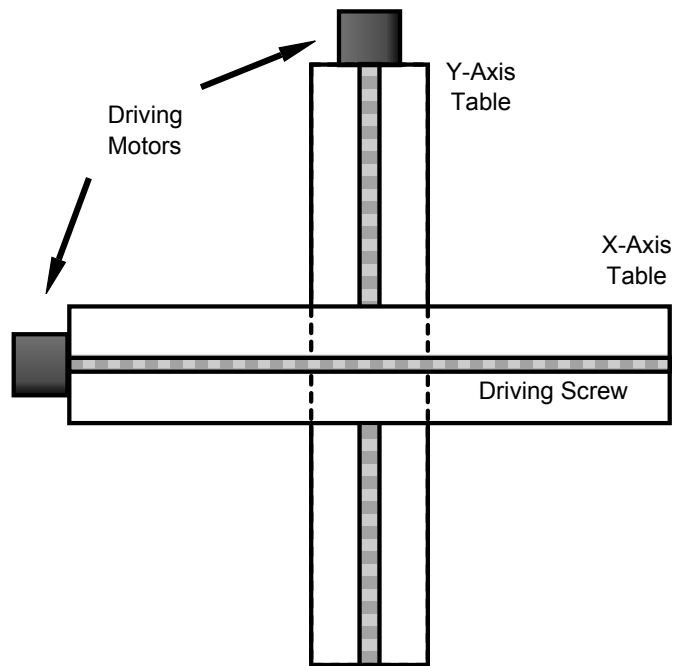


**Figure 2.8:** A schematic of the layout of the actuator system in use with the near field scanner. The system stands upright and suffers from a loss in load capacity as a result

### 2.2.1 XY Scanner Configuration

The scanner system in use consists of two linear positioning tables mounted together. Each table has a ball and screw configuration in which a ball-bearing roller is moved via the turning of a lead screw. The lead screws are powered by two individual stepper motors, one for the x-axis and another for the y-axis. The motion of the carriage on each axis is facilitated by two supporting ball-bearing rail slides. These slides allow for low friction and precise linear motion. The layout of the actuator system can be seen in figure 2.8. The back of the x-axis table is mounted to the y-axis carriage. This results in the y-axis having to support much more weight than the x-axis when standing upright. Both axes also utilise lead screws of different pitch and for this reason a full rotation of the y-axis screw results in a greater linear displacement than the x-axis; 2.52 mm/r for the x-axis and 5.12 mm/r for the y-axis.

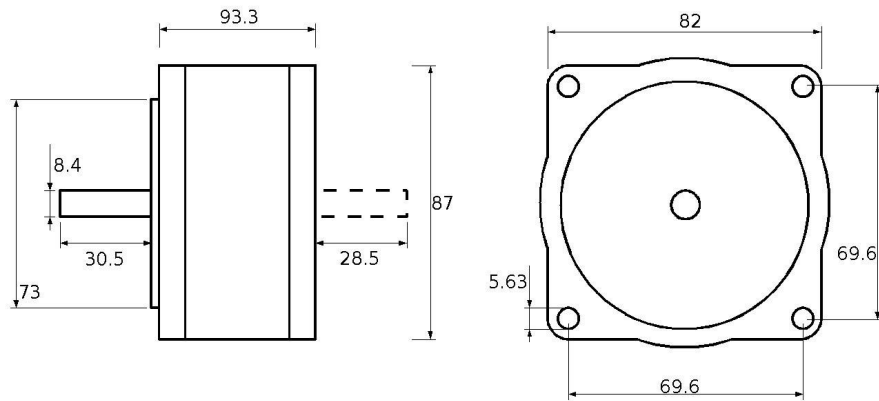


**Figure 2.9:** Shown here is a schematic diagram of one of the Astrosyn motors used to drive the lead screw of an axis. The model in use has no rear shaft extension and cannot facilitate a positional encoder.

## 2.2.2 Stepper Motors and Driver Boards

One full revolution of a stepper motor is divided into a large number of discrete steps. As the motor only has a set number of discrete positions, the rotation of the motor can be controlled accurately without any positional feedback. The turning of the motor is caused by the energising and de-energising of successive ‘toothed’ electromagnets. For a stepper, the repeatability and accuracy of rotation is generally of the order of 3 % and is non-cumulative from one step to the next. Stepper motors can be implemented either as bipolar or unipolar devices.

Unipolar motors have two windings per phase, one for each direction of the magnetic field. This arrangement allows for the magnetic poles to be switched without switching the direction of the current. Bipolar motors have only one winding per phase and thus a change in the direction of the current must be facilitated in order to switch the poles. The implementation of the driver circuit for a bipolar motor is more complex but make better use of the windings. As a result of this they are more efficient and have better torque than unipolar motors of the same size.



<b>Step Angle</b>	1.8°
<b>Step Angle Accuracy</b>	5 %
<b>Holding Torque</b>	0.23 Nm
<b>Detent Torque</b>	0.016 Nm
<b>Rotor Inertia</b>	1300 gcm <sup>3</sup>
<b>Mass</b>	2.4 kg
<b>Phase Current Rating</b>	4.6 A

**Table 2.1:** Table of the characteristics of the Y259/Y260 Astrosyn stepper motors, used to drive the XY scanner table.

Both the x-axis and y-axis are controlled by a single Astrosyn bipolar stepper motor (see figure 2.9). The motors drive the two separate lead screws which convert their rotary motion into a linear displacement. Both motors step 200 times in one revolution resulting in a single step angle of 1.8°. This step angle, in conjunction with the pitch of each lead screw, translates into a linear displacement of 0.0126 mm/step in the horizontal and 0.0256 mm/step in the vertical. These displacement values can be halved by operating both motors in half-stepping mode.

In order to drive the Astrosyn stepper motors two V10745 bipolar stepper motor drive boards are used. In the original system setup these boards needed to be operated independently and thus both axes could not be adjusted simultaneously.

As well as the XY scanner already mentioned another stepper motor driven translation stage is also in use. This translation stage was salvaged from previous experimentation on a Golay cell detector, performed by Mr. Stuart Kehoe here at NUI Maynooth [21]. This z-translation stage is used for adjusting the distance between the transmitting and receiving heads. The driving of the stage is performed by a 7.5° Premotec stepper motor in conjunction with a 50 : 1 gear-

<b>Motor Supply</b>	+15 V to +35 V
<b>Logic Supply</b>	+15 V to +24 V
<b>Max Input Current Per Phase</b>	3.5 A
<b>Logic Voltages (Low/High)</b>	0 V to +2 V / +9 V to +30 V
<b>Monitor Outputs (Low/High)</b>	+1 V / +24 V
<b>Operative Temperature Range</b>	0 °C to 40 °C

**Table 2.2:** Characteristics for the V10745 bipolar stepper motor drive boards.

box supplied by McLennan Servo Supplies. This set-up, along with a micrometer screw gauge, allows for control of the position with 0.0002 mm resolution.

### 2.2.3 Other Components

In order to avoid damaging the components described earlier in this section it is necessary to prevent the XY scanner from moving outside its operational range. In order to implement this, slotted optical switches are incorporated into the actuator system. The printed circuit boards created for this purpose use Omron EE-SM3B transmissive photomicrosensors and the circuit used is shown in figure 2.10.

If either axis approaches its limit, a metal fin passes through the centre of a slotted optical switch and blocks the path of an IR beam. The drop in signal is communicated to the computer which then cuts the driving signal to the motors. This redundancy system along with the V10745 driver cards are connected to the controlling PC via a control box. With the current set-up only one of the motors can be operated at a given time. The control box facilitates the switching between the two driver cards. This device handles all the information sent to and from the cards, as well as feedback from the slotted optical switches. The

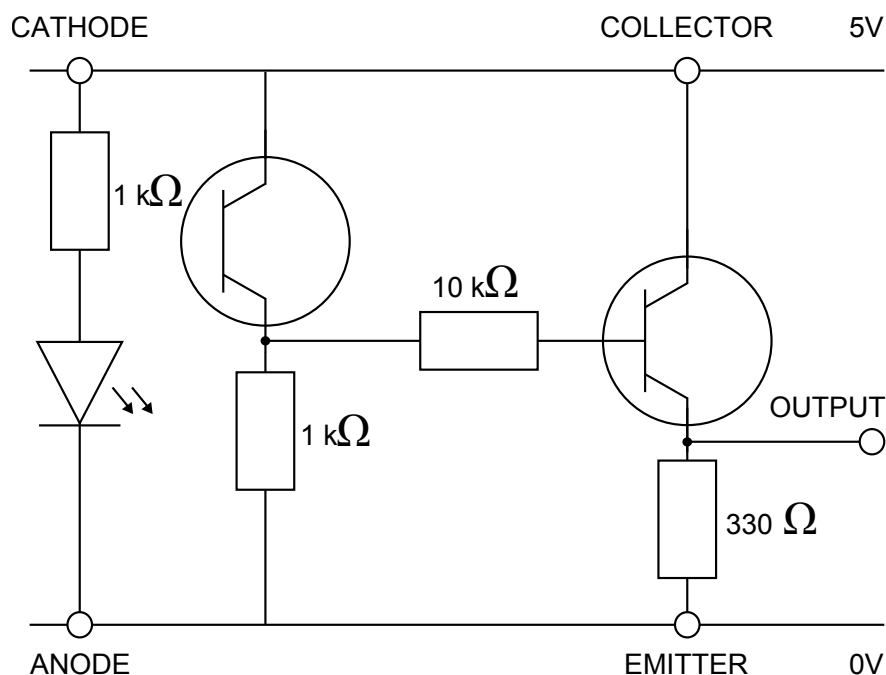


**Figure 2.10:** Circuit diagram for the PCB implementation of the slotted optical switches. These PCBs are used as limit switches to prevent the actuator system from moving outside its operational range.

clock lines, direction lines and power lines for the motors, along with logic lines for the limit switches are all generated here.

## 2.3 Measurement Method

For most of our measurements it is necessary to map out a grid of information on a two dimensional plane in order to understand how a beam evolves as it propagates. The receiving converter head that is mounted on the XY scanner must be moved accurately from position to position on the grid. The resolution of the scan is decided on before measurement begins, with the minimum possible being 1 halfstep of the motor. This constitutes a different linear displacement in each axis; 0.0063 mm in the x-axis and 0.0128 mm in the y-axis.

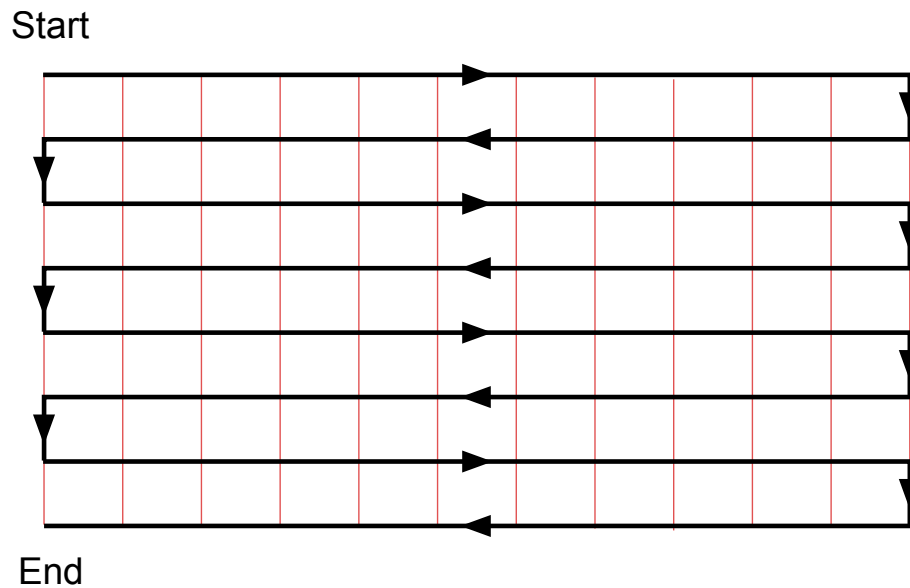


**Figure 2.11:** The standard raster scan pattern used for taking a measurement.  
 In this particular case the horizontal axis is the minor axis.

With the current set-up, the motors move in a start-stop fashion, with a velocity of 300 steps/s (or 1.89 mm/s in the horizontal and 3.84 mm/s in the vertical). The operational distance for both axes exceeds 300 mm, meaning the travel time from one end of the scanner to the other is of the order of minutes instead of seconds. As a result, the chosen resolution of a scan can have a dramatic effect on the length of time it takes to complete a full grid measurement.

When a scan is being performed, a cut is taken through the minor axis of motion and then the major axis of motion is adjusted. It would be very time consuming to reset the minor axis every time the major axis is adjusted so this is not done. When a slice has been completed, regardless of the resolution, the major axis is instantly adjusted and the next row of the raster scan is performed in reverse. This process is continued until the full grid has been completed. An example of one of these scan patterns can be seen in figure 2.11.

## 2.4 Improving the Scanning System

As the overall goal of this project is the optimisation of the scanning system there are a few issues that need to be addressed. The most prominent of these would be the overall efficiency of the scanner. With the most common use of the XY scanner being the performance of two dimensional scans, a decrease in travel time from point to point would dramatically increase the speed at which a measurement could be performed. Currently, the motors that are in use with the scanner are not being used to their full potential and this needs to be corrected.

The development of a new motion control system for the purpose of unlocking the potential of the motors is necessary. While this is being undertaken it would also be useful to develop other systems that would allow for more accurate tracking of the position of the scanner. While the redevelopment of the scanner is being performed, it would be sensible to also develop an accurate step by step alignment procedure as the current methods are not satisfactory. This however, will not be discussed until chapter 4 of this thesis.

## 3 System Upgrades and Vibration Analysis

As part of this project, it was decided that the current set-up of the scanning system needed to be upgraded. The main goals of the upgrade were to increase the precision and efficiency of the scanner. A complete overhaul of the motion control system was necessary to achieve these goals. This included the installation of new stepper motors and driver boards along with the addition of position encoders.

Once the upgrades were completed it was noticed that a higher level of low and high frequency mechanical vibrations were being evoked in the scanner. The low frequency vibrations were seen to be causing problems with measurements by introducing positional errors. The manifestation of the high frequency excitations was seen in the form of a higher level of acoustic noise.

These excitations needed to be studied in order to determine ways of decreasing them while not affecting the increased efficiency of the system. Originally a method of displacement analysis was used in an attempt to determine what positional offsets were being introduced by the low frequency vibrations.

Subsequent to this a Fourier analysis of the vibration was performed in order to determine the specific resonant frequencies of the system. Understanding what frequencies are being excited the most is key to determining what the main contributing factors to the excitations are.

## 3.1 System Upgrades

The original set-up of the scanner involved a rudimentary approach to motion control with the motors moving in a start-stop fashion. This type of motion control involves the instantaneous movement of the motors at a maximum velocity of 300 steps/s (or 1.89 mm/s in the horizontal and 3.84 mm/s in the vertical). This implementation fails to use the full potential of the stepper motors which are capable of moving at 10000 halfsteps/s with no load. The low stepping frequency results in time consuming measurements due to a relatively long travel time from position to position. In order to reduce this travel time a National Instruments motion control card (NI PCI-7334) was installed to allow for more complex motion trajectories to be programmed.

Many other upgrades will also be discussed in this chapter, including new translation stages and safety features. The system, when upgraded, presented us with new problems in relation to measurement precision. The more powerful driving of the system that was facilitated by the new motion control system introduced larger amounts of vibration in the scanner structure.

As well as discussing the upgrades themselves, this chapter will also be used to outline the methods used for vibration analysis. After showing the attempts to understand the vibration levels and causes, the attempts to reduce the excitations though adapting the structure and motion profiles are also chronicled.

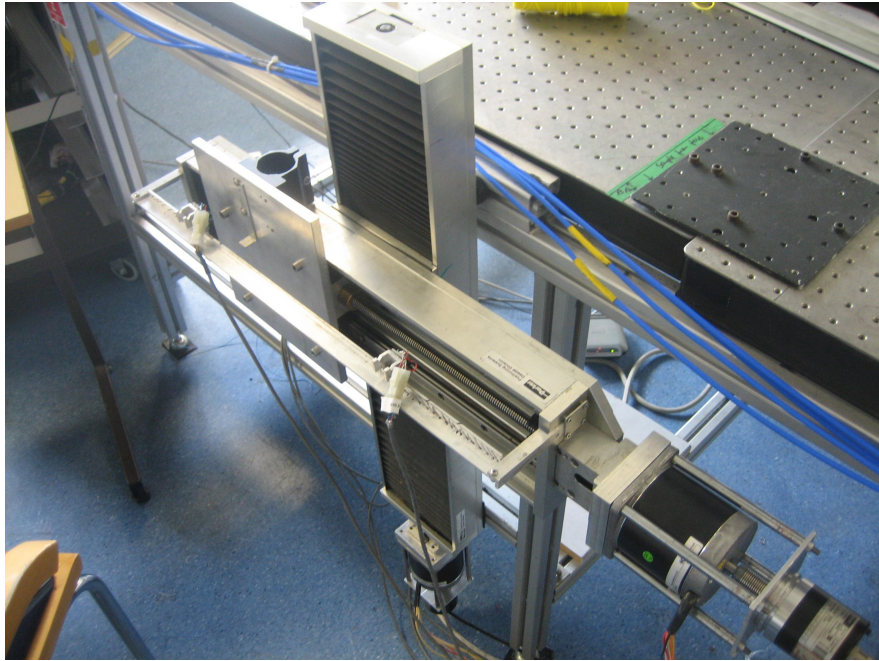


**Figure 3.1:** An image of the actuator system. These two translation stages are used to move the receiving converter head from point to point in order to map out a grid of complex amplitudes encompassing an entire propagating beam.

### 3.1.1 Motion Control Upgrade

Possibly the most important upgrade to the system was the installation of the National Instruments PCI-7334 motion control card. This hardware device allows for fully programmable motion control for up to four independent axes of motion. The card also has dedicated I/O lines for feedback controls such as limit and home switches. Full-stepping, half-stepping and micro-stepping of the individual motors is handled by the individual stepper motor drivers (415-8544 from McLennon). For the new configuration, the stepper motors are operated in half-stepping mode.

With this new hardware it is possible to programme complex trajectories using stepper motors by facilitating the change of motion parameters such as acceleration, deceleration, maximum velocity and jerk. The signals being sent to each



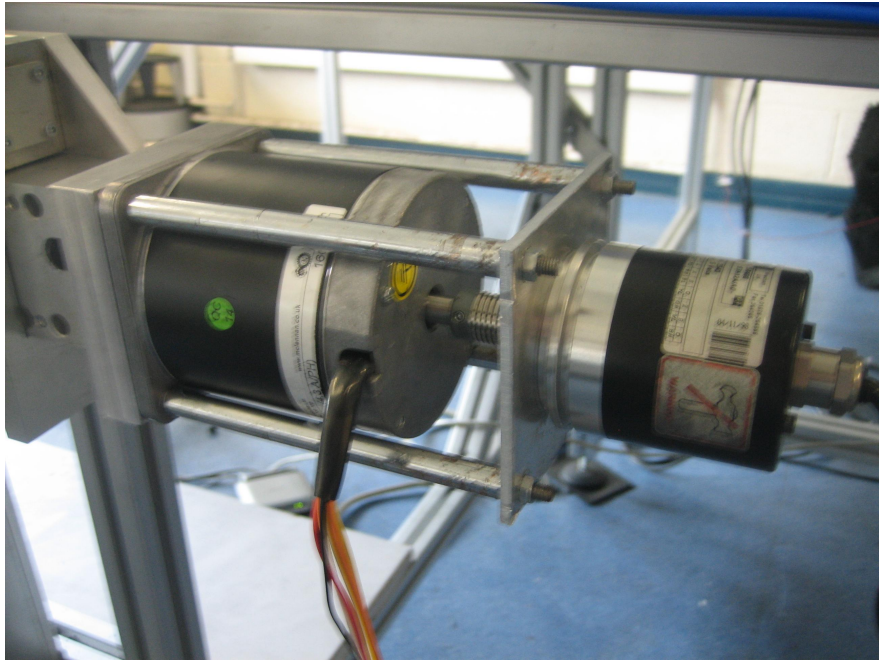


**Figure 3.2:** An image of the differential encoders in use with the XY scanner system. These encoders are attached to the drive shafts via the rear shaft extension of the new stepper motors.

motor are conditioned by another National Instruments device, the universal motion interface (UMI-7774). The interface allows for the simultaneous handling of motion control and feedback from up to four separate axes, as well as additional system data.

With the original system set-up, the tracking of the position of each axes could only be performed by recording how many steps the motors were instructed to move. There was no facility for keeping track of any positional errors that might occur and this was deemed to be unacceptable. In order to constantly keep track of the exact position of both the x and y axes, two rotary encoders were incorporated into the system. One of these encoders is pictured in figure 3.2.

There are two types of rotary encoders, absolute and differential. Absolute encoders output a unique digital signal for each possible angle that the shaft can be rotated at. Incremental encoders need to have a zero point defined and pulse

<b>Max Frequency</b>	150 kHz
<b>Current Consumption</b>	50 mA
<b>Power Supply</b>	5 – 24 V
<b>Torque</b>	5 N-cm
<b>Speed</b>	6000 RPM max

**Table 3.1:** Table of the characteristics for the E series incremental encoders from Hohner

every time that the shaft rotates by a certain angle. These pulses are counted and used to calculate the exact position away from the zero point. Incremental encoders generally have a much better resolution than absolute encoders and for this reason were chosen for the near field scanning system. It should be noted that these incremental encoders, unlike their absolute counterparts, have no memory of the position they were in once powered down.

Unfortunately the stepper motors originally in use for both axes did not have the rear shaft extension needed to mount positional encoders on to the system. Two new stepper motors with a rear shaft extension were purchased. These new motors are from the McLennon HSX series and have the same specifications as the original motors.

With the new motion control system in place, a large increase in the maximum velocity of the movable receiver was seen. Originally the maximum velocity was 300 steps/s, but with the new system this was increased as far as 8500 halfsteps/s resulting in much shorter travel times when travelling relatively large distances.

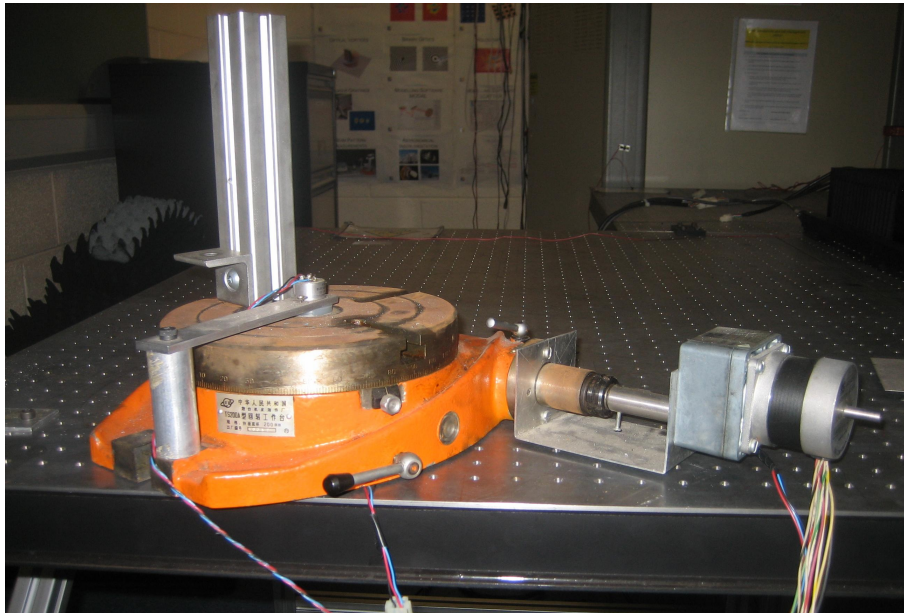


**Figure 3.3:** An image of the stepper motor driven rotary translation stage. This stage is used to automate the rotation of an optical component in order to perform measurements at different orientations.

### 3.1.2 Additional Translation Stages

As the new motion control hardware (PCI-7334 and UMI-7774) allow for the simultaneous control and feedback from four separate axes two additional translation stages were incorporated into the system. These extra stages are used in the testing of more complex optical systems.

The rotary translation stage (figure 3.3) is used to rotate a component in an optical system. For example, when performing measurements on a piece of dielectric it is useful to be able change the angle at which a propagating beam intersects it. It is possible to determine the refractive index of the material by looking at how the reflection and transmission coefficients change as the angle of orientation of the dielectric changes. Making use of the rotary translation stage allows us to completely automate a measurement of this kind.



**Figure 3.4:** An image of the new z-axis translation stage. This stage is usually used to change the distance between transmitter and receiver to investigate standing wave issues.

The new z-axis translation stage (figure 3.4) has a much larger range than its predecessor which was adapted from the Gunn diode apparatus. This extra stage is a large linear table which can be placed on the optical bench. The table itself is moved by an AC servo motor. It is very useful for us to be able to adjust the distance between transmitter and receiver in a particular optical system and this is what the z-axis translation stage is predominantly used for. The ability to change the distance allows us to investigate and correct for any standing waves that may be present in an optical system.

### 3.1.3 New Safety Features

The new z-axis translation stage is a lot more powerful than any other part of the motion control system. Any mechanical system with moving parts presents a hazard for persons performing experimentation but the AC servo powered table is much more dangerous than any of the other equipment in use. For the purpose of safety it was deemed necessary to prevent users from accessing the optical bench while the system is in motion.

An emergency stop button was already in place next to the computer that is used to send commands to the scanner. It was decided to set up a safety cordon around the entire optical bench that would not only limit access to the optical bench but also add the ability to perform an emergency stop at any point in the vicinity of the optical bench.

The motion control card has an emergency stop function that cuts the drive signal being sent to the motors when its digital input transitions from low to high. When the safety cordon is in place there is a constant low signal being sent to the emergency stop connection on the card. If the cordon is broken the signal transitions from low to high and the motors immediately stop if in motion.

With the original implementation of the safety cordon, a serious shortcoming was noticed. As the motion control card is only sensitive to the transition from from low to high (edge) it is not aware of the current state of the system. This allows for the motion control system to be reset and operated even if the cordon was not in place. There is no issue if users always ensure that the safety cordon is in place before beginning a measurement, but relying on this for a critical safety feature is not acceptable.

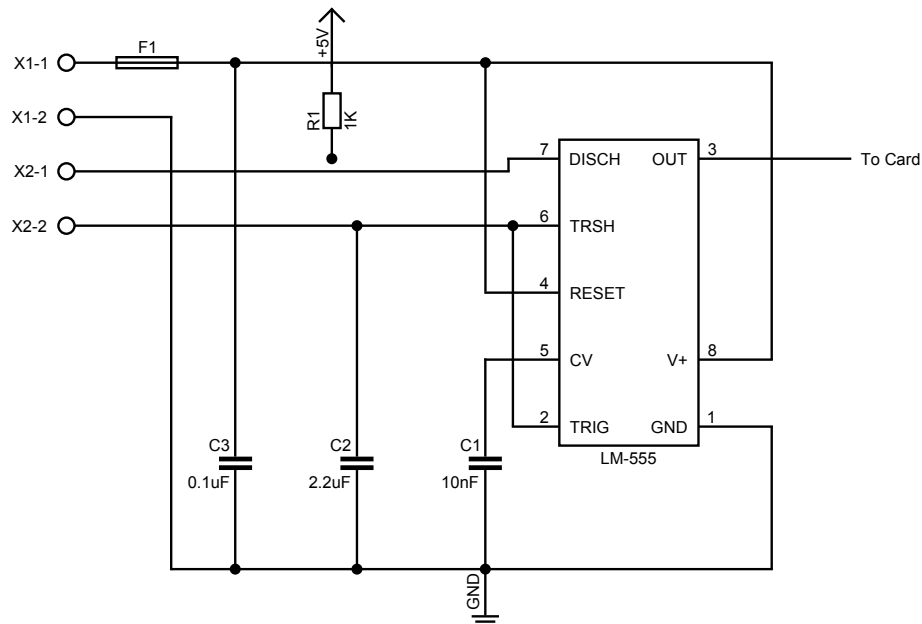


**Figure 3.5:** A circuit diagram of the PCB created to supply a constantly oscillating signal when the safety cordon is tripped. This circuit fixes the shortcomings of the original safety features for the optical bench

To address this issue, a small circuit was devised containing an LM-555 oscillator chip (figure 3.5). The output of this circuit is sent to the emergency stop of the motion control card. When the safety cordon is tripped, a constantly oscillating signal is sent to the card which prevents the motion control system from being operated until the safety cordon is back in place. This has proved successful since its implementation as access to the optical bench while the motors are powered is no longer possible.

### 3.1.4 Problems due to the Upgrade

In order to reduce reflections from the scanner structure itself, the receiving frequency converter head has always been mounted on a long vertical shaft. With the new motion control system in place and the scanner now being driven with

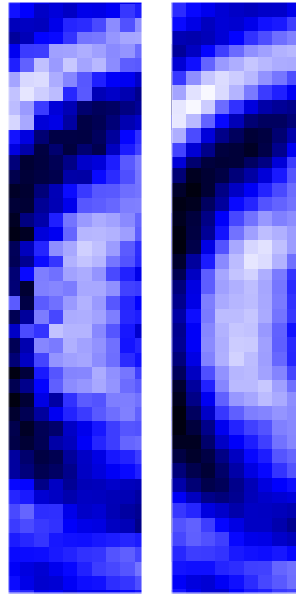


**Figure 3.6:** Shown is a comparison of two measurements taken using the near field scanning system. On the left we see a scan taken with no delay between movement from point to point on the grid and on the right we see the same scan with a one second delay.

more force a problem arose with the scanner.

A noticeably larger amount of vibrational excitations were seen in the scanner structure and also in the vertical extension shaft that the receiver head is mounted on. There are many possibilities as to where the vibrations are coming from. The resonant frequency of the structure, the length and rigidity of the vertical shaft and the impulse that the system is subjected to could all add to the level of vibrations.

While taking measurements, the effect that the vibrations were having could be seen through a "streaking" effect which is shown in figure 3.6. Consecutive rows seem to be out of alignment with each other and the suspected cause of this was a lag in movement between the top and bottom of the vertical shaft.

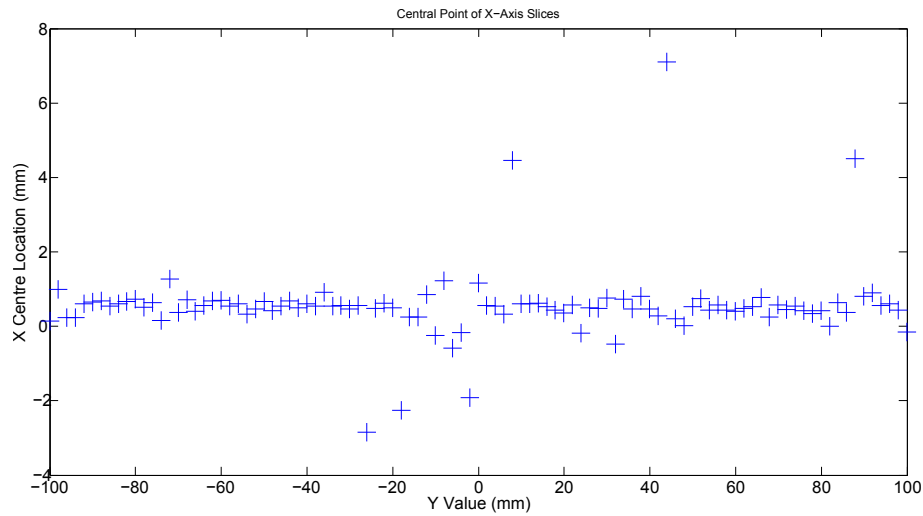


**Figure 3.7:** A plot of the calculated centre point of 101 horizontal cuts through a beam. These values are plotted against their positions on the vertical axis. By calculating the standard deviation we can estimate what effect the streaking is having on our pointing accuracy.

Figure 3.7 shows how, upon analysis of the streaked data, the centre point appears to move. By looking at the standard deviation of this data set we can recover the approximate pointing inaccuracy that is caused by the streaking. For this measurement we calculate a value of 1.02 mm.

A temporary solution to this problem was to introduce a delay between the movement of the head and the recording of the complex amplitude. This process allows for any vibration in the system to be damped at the cost of time. As one of the main reasons behind the upgrade was to increase efficiency, having to add a delay between each step seemed counter-productive and a full analysis of the vibration was undertaken with the aim of understanding and reducing the excitations.



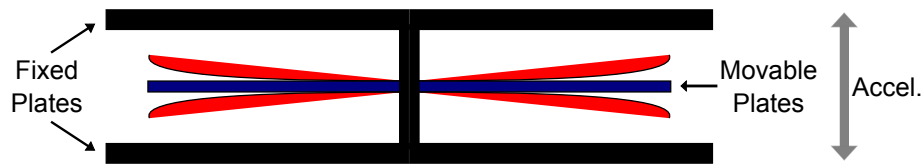


**Figure 3.8:** Schematic showing how one axis of the LIS3102AS4 commercial accelerometer operates. As the device undergoes an acceleration the distance between the fixed and movable capacitor plates changes.

## 3.2 Analysis of Converter Head Displacement

The faster movement of the W-band converter head mounted on the scanner is seen to evoke higher levels of vibration in the system than were present in the original set-up. This increase is mainly due to increased power at which the system is being driven and the long metallic shaft that was installed to reduce reflections.

A study was undertaken to determine if the level of these vibrations would cause a significant decrease in the signal-to-noise ratio of the W-band measurements. With the new motion control system it is possible to program acceleration, deceleration and maximum velocity parameters as well as a smoothing co-efficient to achieve a desired movement profile. It would also be desirable to gain an understanding of how these parameters affect the excitations.

These movement profiles once designed can be programmed and executed by the Ghost 2 motion control software developed by Dr. Marcin Gradziel. Ghost 2 also allows for the addition of a wait period between each step of a scan to be set. The value is usually set to be quite low due to it adding a significant amount of rest time to higher resolution scans. Ideally the vibrations should be at a low enough level to avoid using any wait period at all.

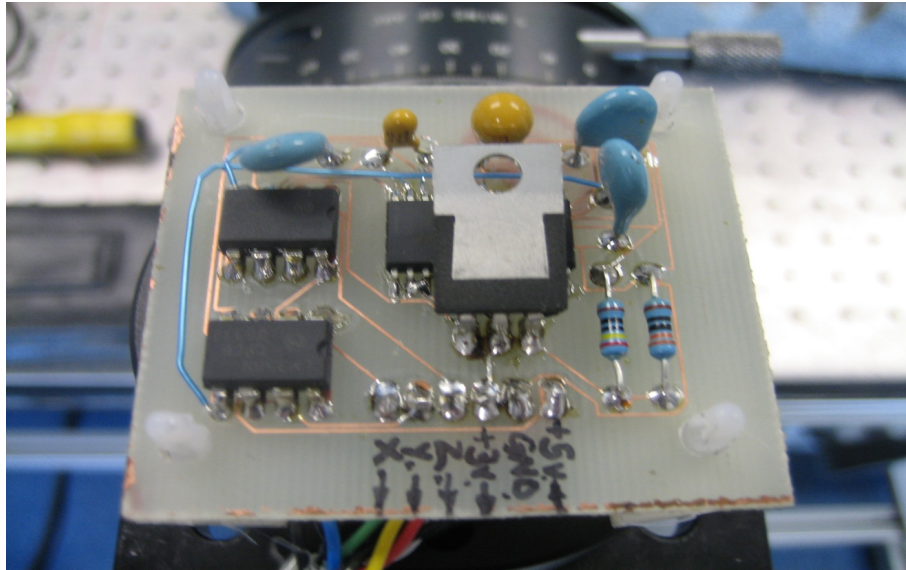


**Figure 3.9:** An image of the printed circuit board created for the LIS3102AS4 accelerometer. For most measurements this PCB is mounted underneath the moving frequency converter head.

In order to extract the levels of vibrations in the system a 3-axis commercial accelerometer (LIS3102AS4) was mounted underneath the converter head. This accelerometer is a MEMS (Micro-ElectroMechanical System) device, meaning that it uses the movement of internal mechanical components in order to adjust its electronic output.

For each of the 3 axes of the accelerometer, there is a set of two parallel plate capacitors connected in a bridge. The outside plates are fixed in position while the inner plates are free to be displaced with respect to acceleration (figure 3.8). The device outputs a voltage that is related to the acceleration in each axis [22]. Data from the accelerometer is collected using a National Instruments DAQ and processed using LabVIEW. There are 4 channels of data, the 3 axes of the accelerometer and the supply voltage.

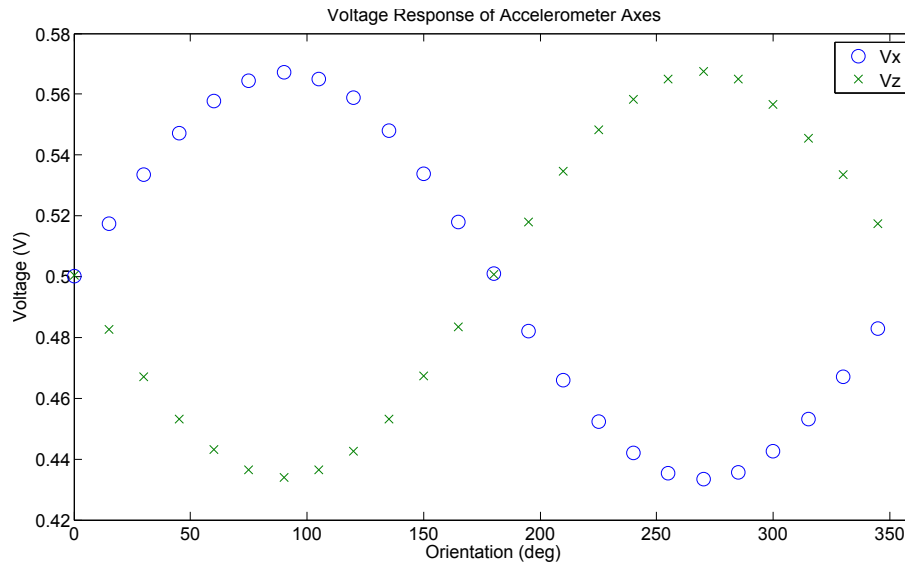


**Figure 3.10:** Plot showing the change in output voltage for the y and z axes of the accelerometer as their orientation is changed. As acceleration due to gravity is a known quantity it is used as the calibration standard.

The response of each axis of the accelerometer is defined by equation 3.1:

### 3.2.1 Calibration of Accelerometer

Before any measurements were taken with the accelerometer its operation was verified and the output signals calibrated. This was performed using a simple device constructed out of two rotary translation stages. The output voltage corresponding to each axis of the accelerometer was recorded for different angles of orientation around a sphere.

As only two rotation stages were being used it was only possible to rotate the accelerometer around two axes and then the mounting of the device needed to be changed. Figure 3.10 shows the change in output voltage for the y and z axes as the accelerometer was rotated through  $360^\circ$  in the y-z plane ( $15^\circ$  intervals).

For the purpose of calibration the output voltage was normalised to the supply voltage of the chip.

$$y = A_0 + A_1 \sin\left((x - A_2)\frac{\pi}{180^\circ}\right) \quad (3.1)$$

Where  $A_0$ ,  $A_1$  and  $A_2$  represent the mean, the gain and the angular offset all normalised to the supply voltage. The values for each of these variables are used to calculate the acceleration on a particular axis.

### 3.2.2 Position Profile Extraction

In order to extract an acceleration profile from the data obtained, the measured voltage from each axis must be processed using the values for the mean and gain from the calibration data. This measured acceleration is defined by equation 3.2;

$$A_{meas} = \left( \left( \frac{V}{V_{supply}} \right) \left( \frac{1}{A_1} \right) - \left( \frac{A_0}{A_1} \right) \right) g \quad (3.2)$$

Integrating the acceleration profile twice with respect to time should give a value for position however when this is carried out a problem arises. A graph of the position against time shows that it is completely dominated by a parabola (with extreme and unrealistic values for displacement).

This parabola effect is caused by the double integral of a constant present in the measured acceleration. The constant is a voltage offset which could arise due to multiple reasons. The offset may come from inaccuracies in the amplifiers on the chip or even imperfect calibration. We must take this into account for the

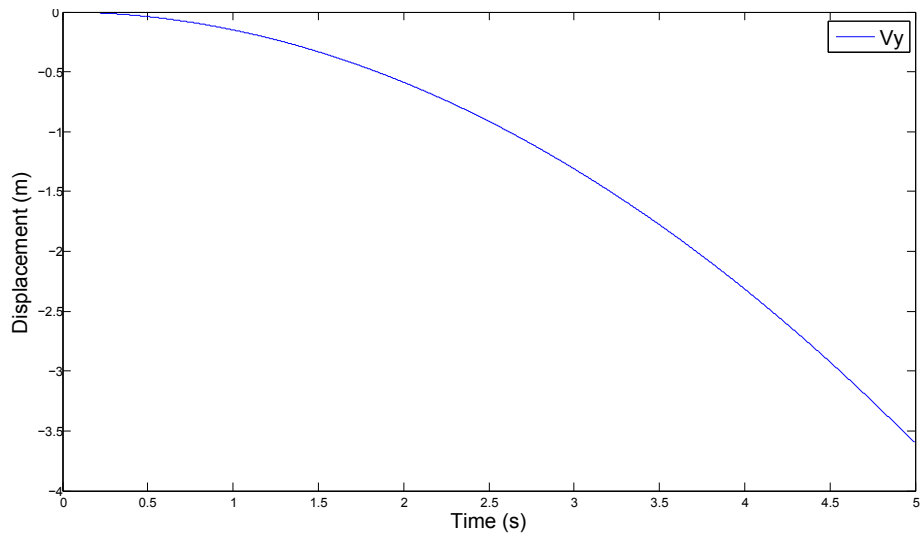


**Figure 3.11:** A plot of the displacement in the y-axis as we move horizontally. An unrealistically large value of displacement is shown as a result of the parabola effect from the voltage offset.

real position profiles to be determined. In order to determine the real measured acceleration we follow the process outlined in equation 3.3 and equation 3.4.

$$a_{meas} = a_{real} + \Delta a \quad (3.3)$$

$$x = \int_0^t \int_0^t (a_{meas} - \Delta a) dt \quad (3.4)$$

When moving the converter head we know both its initial and final position. A LabVIEW program was constructed that uses a known starting and stopping point for the converter head and then iteratively searches for the correct offset voltage. Using the offset a corrected plot of the position profile can be created as can be seen in figure 3.12.

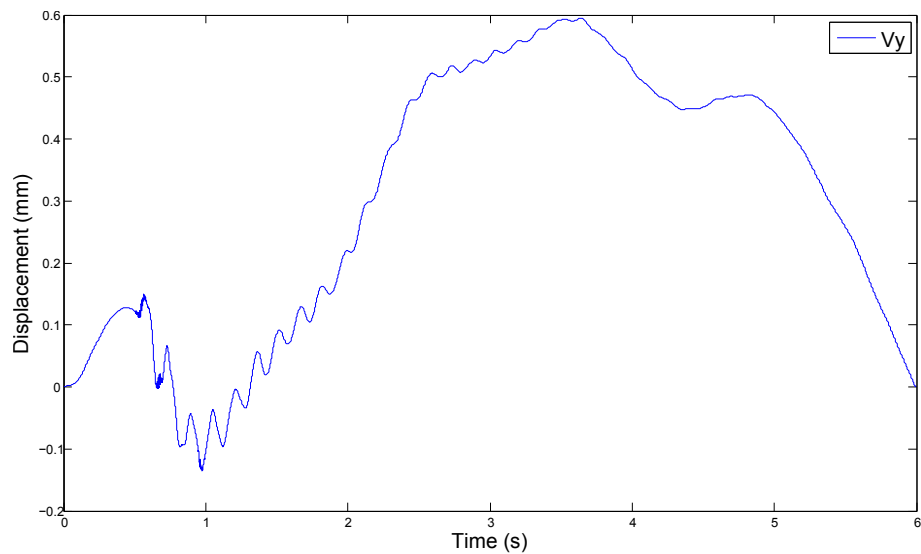


**Figure 3.12:** In this plot the data from figure 3.11 has been processed. The known initial and final position are used to determine the voltage offset and is subsequently used to remove the parabola from the data.

### 3.2.3 Conclusions, Problems and Possible Solutions

For all of the position profiles it can be seen that the vibration levels are quite low. In fact they are much lower than expected as the vibrations are physically visible but the processed results conclude that they are only be a fraction of a millimetre.

Due to the length of the shaft that the W-band converter head is mounted on it was expected that the converter head should lag slightly behind the shaft as the scanner accelerates and then would overshoot the shaft as the scanner comes to a halt. This cannot be seen in the position profiles of the x-axis when moving horizontally.

In figure 3.12 the motion during the collection of data only lasted for roughly two seconds. The DAQ was allowed to collect data for a period of time longer than the motion after the scanner had come to rest. However, the plot does not show

the scanner coming to rest until the end of the scan. I believe that this shows that our method of determining the voltage offset is flawed.

In fact it may well be the case that the accelerometer itself is not accurate enough to determine the displacements. Due to these discrepancies it is reasonable to assume that the calculation of the position profiles in this way is overall inaccurate and another method should be used.

### 3.3 Spectral Analysis of Vibration

In order to determine quantitatively the contributing factors to the vibration in the scanner system we use spectral analysis. Analysing the spectrum allows us to determine what frequencies are excited the most. Again our data is collected using the LIS3L02AS4 MEMS Inertial Sensor.

	<b>x-axis</b>	<b>y-axis</b>
<b>Max Velocity</b>	8500 steps/s	8500 steps/s
<b>Acceleration</b>	40000 steps/s/s	20000 steps/s/s
<b>Deceleration</b>	40000 steps/s/s	20000 steps/s/s
<b>S-Curve Time</b>	400	800
<b>Dist. per Step</b>	0.00635 mm	0.0127 mm

**Table 3.2:** Table of the motion parameters used for each axis in the original data set.

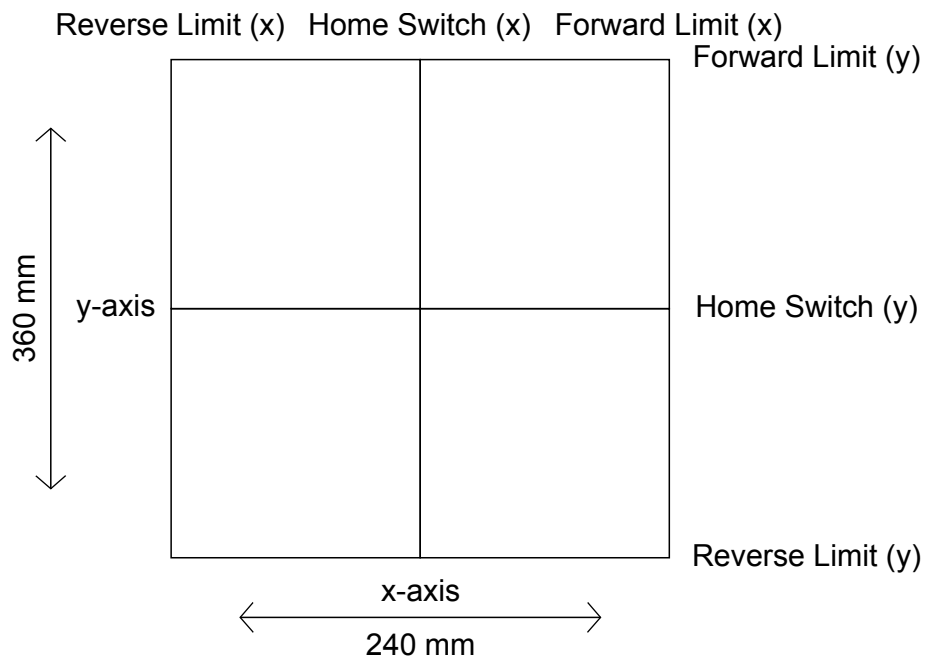


**Figure 3.13:** A schematic of the grid constructed by the six 1-dimensional slice measurements. Each of the lines on the grid represents one of the six slices, though the centre and both extremities for each axis.

Initially a large set of data was recorded to be used as comparative data for any improvements made to the scanning system. With the accelerometer mounted at 3 different points (Under the converter head, on the left side of the structure and on the right side of the structure) data was recorded for the following step-sizes; 0.2 mm, 0.3 mm, 0.4 mm, 0.5 mm, 0.6 mm, 0.7 mm, 0.8 mm, 0.9 mm, 1.0 mm, 1.4 mm, 1.6 mm, 1.8 mm, 2.0 mm, 2.2 mm, 2.4 mm, 2.6 mm, 2.8 mm, 3.0 mm

For each step-size, data was recorded for six different 1-dimensional slices, three horizontal scans and three vertical scans (see figure 3.13). These scans are performed across one axis as the other is kept stationary at either the central position or at one of the extremities. The structure on which the scanner was originally mounted is not symmetrical so it was important to look at how the levels of vibration in the system change depending on where the scan is being performed.



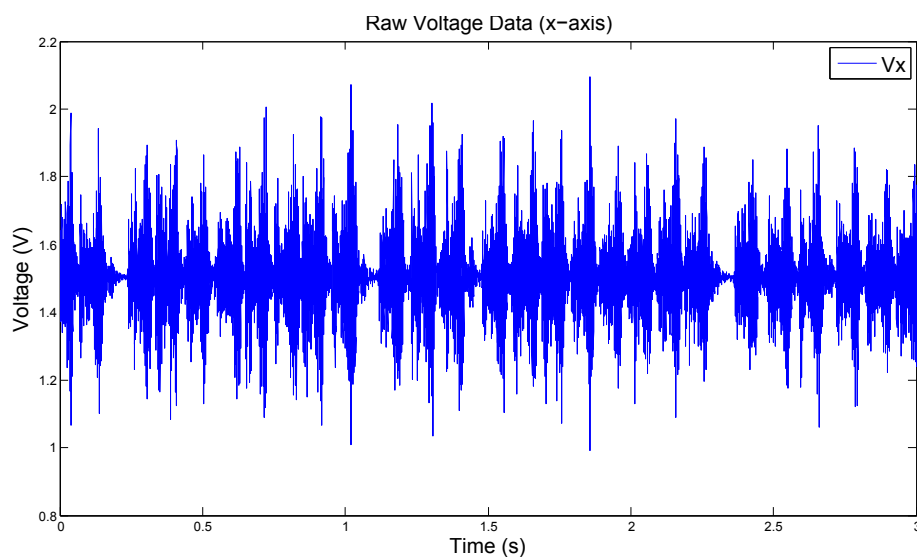


**Figure 3.14:** Raw voltage data from the x-axis channel of the accelerometer. These data were recorded with the accelerometer mounted on the converter head while it moved in the vertical direction. The head moved in 0.20 mm steps

### 3.3.1 Analysis of Original Data Set

Data is stored in binary format as a .tdms file (streaming data). A segment of recorded data can be seen in figure 3.14. This segment shows variation in the output voltage for the x-axis of the accelerometer as the scanner moves in the vertical direction. The data shown is not normalised to the supply voltage of the of the accelerometer circuit as in the previous analysis.

It is also not necessary to process the voltage into units of acceleration. We neglect the actual values of voltage and concentrate on the regularity of excitations. By performing a Fourier transform of the data we convert into the frequency domain. From here we can study the excited frequencies and their harmonics.

The spectral analysis is carried out by a standard VI in the LabVIEW environment. This is used to determine the Power Spectral Density for each particular

frequency being excited. The process of spectral analysis is carried out for all of the original data sets.

With the original mounting of the scanner on a free standing structure, it is necessary to study the vibrations in the structure itself as well as the vibration of the converter head mounted on the scanner. To achieve this the accelerometer PCB was mounted at both extremities of the structure and a full set of data was acquired.

In order to determine what effect the scanner structure was having on vibrations a comparison was drawn between measurements with the accelerometer mounted on the head and on the structure. Figure 3.15 shows the excitations in all three axes for an identical measurement. Each plot compares the level and frequency of the excitations when the PCB is attached either the head or the structure.

In this case the two measurements being compared are for the same vertical scan of step size 0.4 mm. The total power of the excitations is determined by analysing each of plots. It was found that in all directions there was more power in the excitations on the structure than on the converter head itself.

This is most likely due to the free-standing nature of the scanner support structure itself. Along with this the apparent matching of resonances at 660 Hz shows a possible transferal of structural resonances to the head mount. For these reasons, it was decided that the first improvement to be made to the scanner would be the removal of the structure altogether and subsequent mounting of the actuator system directly on to the optical bench.

Once the scanner was mounted to the optical bench, a new set of data was collected in order to see if there had been any improvements. For horizontal

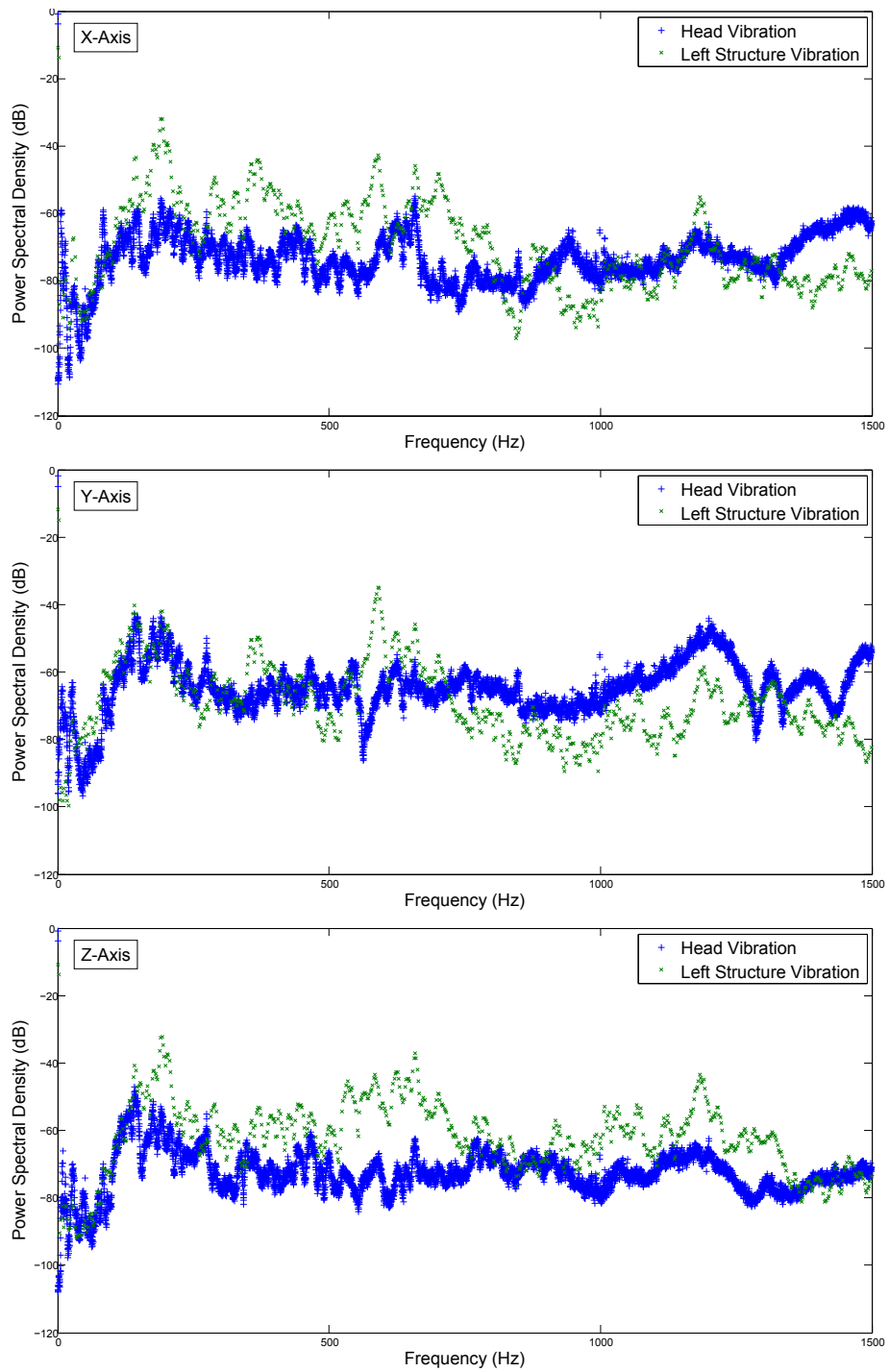


**Figure 3.15:** These three plots show the spectral analysis of the excitations in each of the axes of the accelerometer. In this case we are comparing the vibrations when the accelerometer is mounted on the converter head and also on part of the structure.

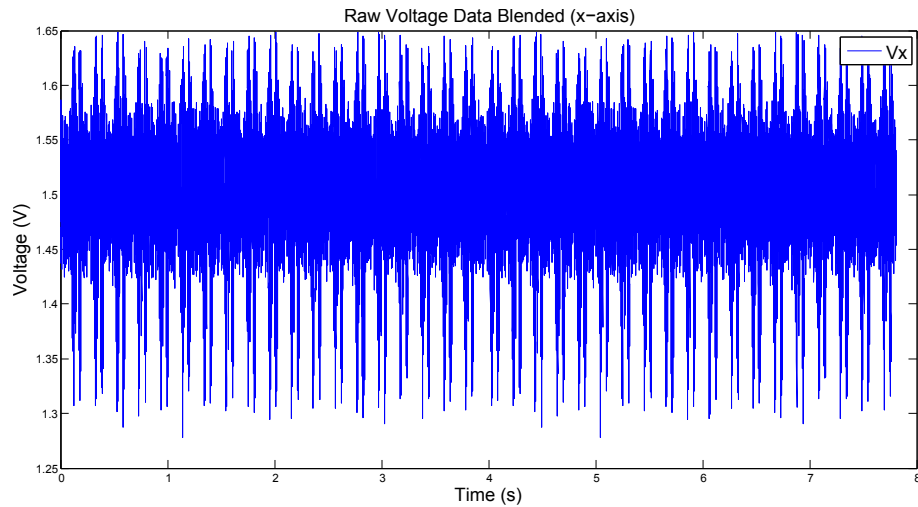


**Figure 3.16:** Raw data from a vertical scan of step size 0.80 mm. These data are recorded from the x-axis channel of the accelerometer. The regularity of the excitations should be noted, this is due to the implementations of the blended motion scheme

movement a global reduction in the total level of vibration was seen, albeit this reduction is quite small ( $< 1\%$  in most cases).

Unfortunately also apparent in the new set of data is a small increase in vibrations when moving in the vertical direction. The increases are only present in the acceleration data for the x-axis and y-axis.

### 3.3.2 Motion Improvement and Further Analysis

Drawing attention back to figure 3.14, it can be seen that the motion is not entirely smooth. The steps for the most part appear to occur regularly but intermittently there is a pause. This pause was actually being caused by a not fully deterministic delay in the software. Using blended motion through LABView it was possible to reduce these irregular stops in the motion.

Blended motion is a process of computing motion on the fly. The original software

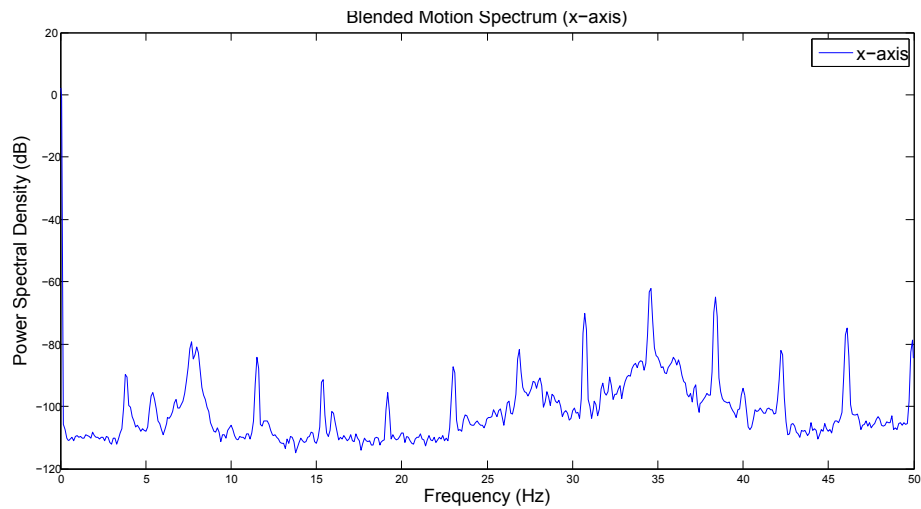


**Figure 3.17:** Spectral Analysis: Vertical Scan 0.80mm (Y-Axis)

implementation involved waiting until the movement from one position to the next was complete before computing the next step. Blended motion allows for the next step to be computed while the scanner is still moving. This allows for a much smoother transition from step to step.

Implementing this may not necessarily improve the vibration in the system, but we would expect that spectral frequency (and the related harmonics) corresponding to the driving of the scanner would become more defined and easier to identify during analysis. Figure 3.16 shows the more regular periodic motion when using the blended scheme.

For this particular case, the motion has a period of about 265 ms from the start to the finish of its 0.8 mm step. With this regularity of the stepping we would expect to see very defined peaks at a fundamental frequency of 3.7 Hz along with subsequent harmonics at 7.4 Hz, 11.1 Hz, 14.8 Hz etc.

In figure 3.17 the spectral analysis of the data from figure 3.16 is presented. The range displayed is restricted between 0 Hz and 50 Hz. Sharp spikes can be seen close to where they were predicted. Inaccuracies in our prediction come from the

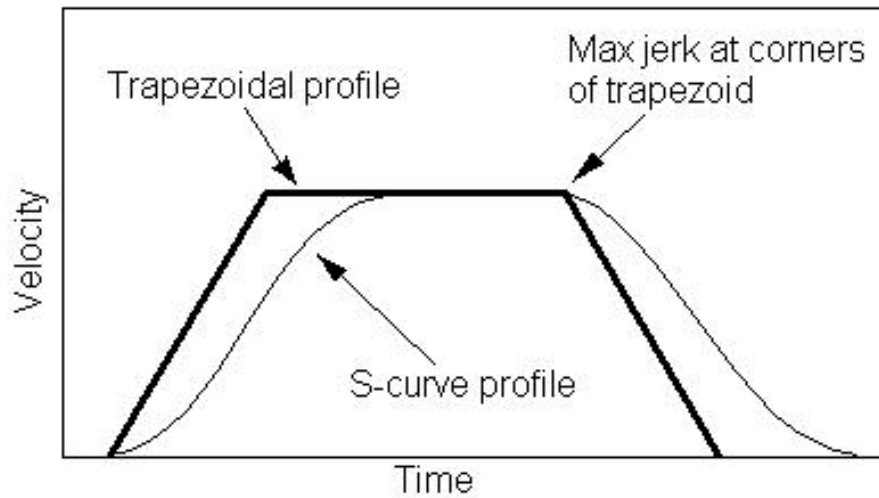


**Figure 3.18:** A comparison between the trajectory for trapezoidal motion and s-curve motion. S-curve motion involves the introduction of the third order derivative of position - the rate of change of acceleration - called jerk.

determination of the exact period of the motion. This is the most likely point of failure of our estimate.

### 3.3.3 Structure of Excitations

There are three different identifiable periodicities embedded in variation in voltage. The most apparent is the large scale structure presented in figure 3.19. This periodicity is caused directly by the starting and stopping of the stepper motor itself as it completes a move. This is without a doubt the most prominent noise in the system, both in low-frequency and in the acoustic range.

The next level of complexity in the signal corresponds to the actual internal stepping of the motor. This has been confirmed by comparing motion profiles for trapezoidal and s-curve motion (figure 3.18).

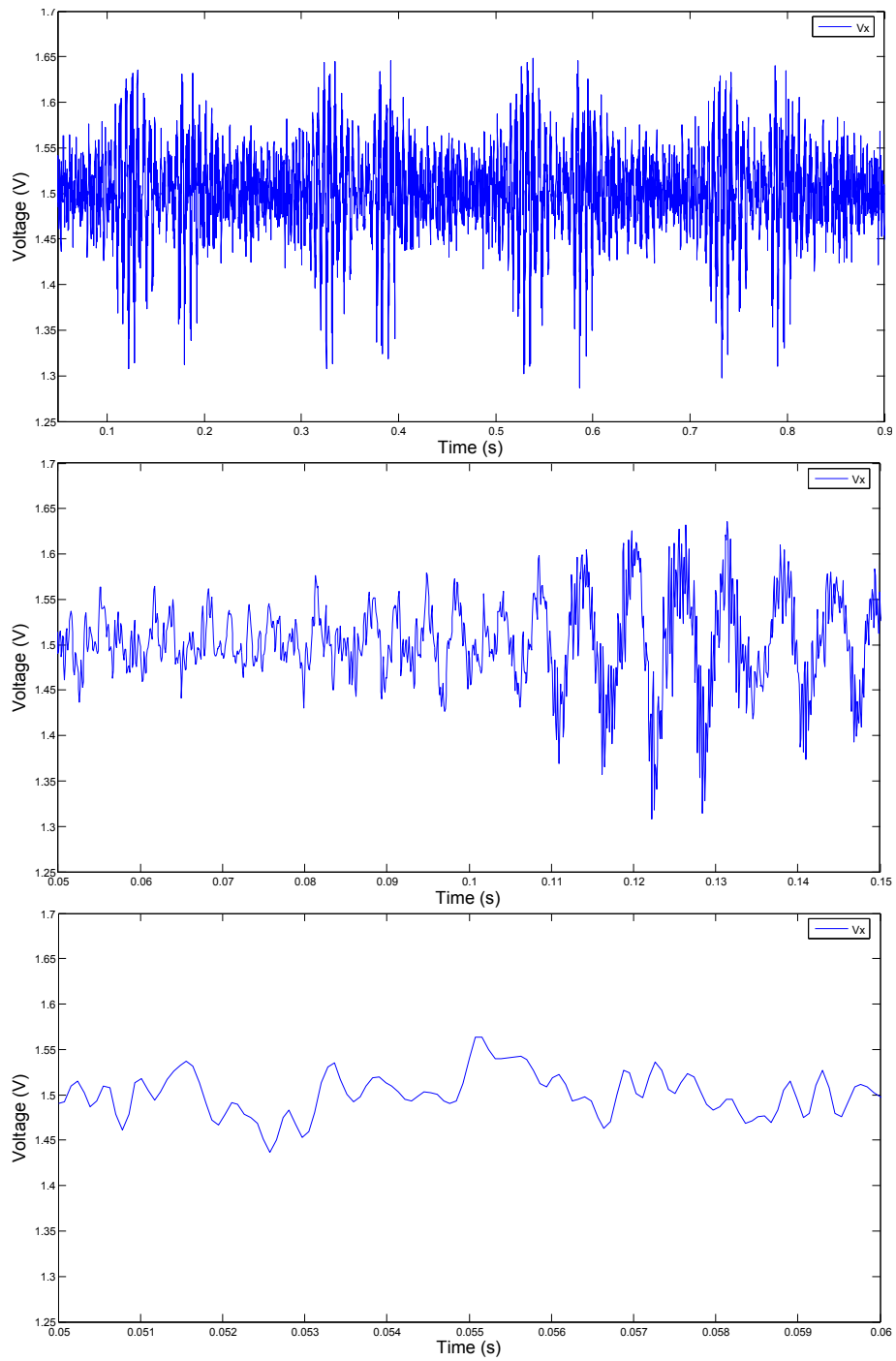


**Figure 3.19:** The same spectrum shown at three different levels of zoom. Here we see large scale structure from the starting and stopping of the motor. The medium and small scale structure is most likely due to the stepping of the motor and differential encoder.

	<b>x-axis</b>	<b>y-axis</b>
<b>Max Velocity</b>	600 steps/s	600 steps/s
<b>Acceleration</b>	4000 steps/s/s	4000 steps/s/s
<b>Deceleration</b>	4000 steps/s/s	4000 steps/s/s
<b>S-Curve Time</b>	2000	2000
<b>Dist. per Step</b>	0.00635 mm	0.0127 mm

**Table 3.3:** Table of the motion parameters used for each axis in the s-curve motion data set.

The rate of change of acceleration, known as jerk, can be adjusted in order to obtain a more smooth motion profile. This parameter has always been set in any axis configuration profile. The introduction of a jerk parameter changes our motion trajectory from a trapezoid to an s-curve.

Due to a bug in the older versions of the NI Motion Assistant, this value is completely ignored if the maximum velocity set is too large. If there is not sufficient time for the motion assistant to ramp the acceleration smoothly the value of jerk will be ignored instead of adjusting the maximum velocity to suit. This issue has been corrected in recent software updates and the use of the jerk parameter may prove to be useful. However, for very small step-sizes this parameter cannot be expected to make much difference.



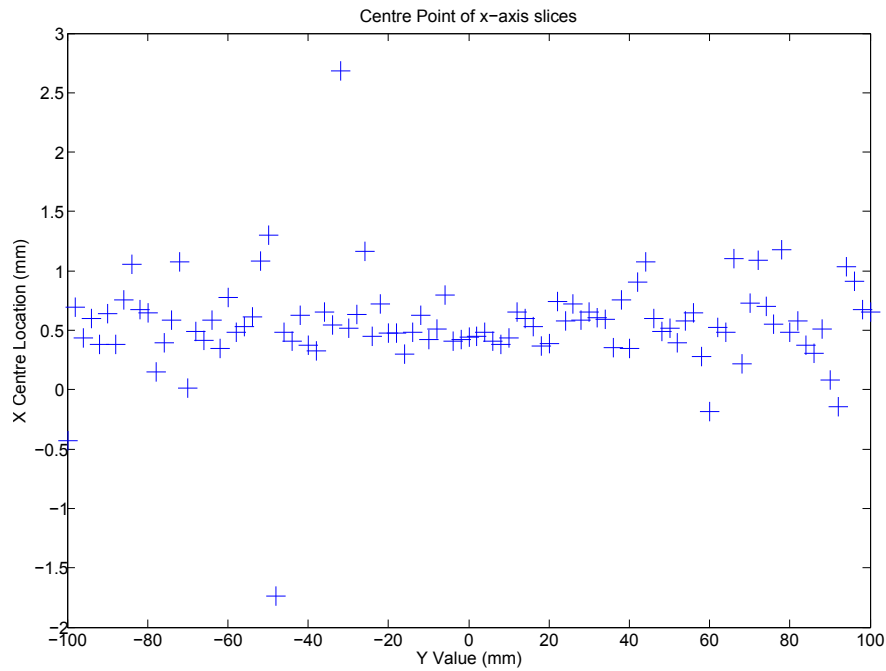


**Figure 3.20:** A plot of the calculated centre point of 101 horizontal cuts through a beam. This plot is a repeat of the analysis performed in figure 3.7. The values for the centres are again plotted against their positions on the vertical axis.

### 3.4 Results and Conclusions

The total level of vibrational noise in the system has not been significantly reduced. With the increase in the rigidity of the scanner and removal of the free standing structure the level of low-frequency vibrations have been reduced. This was our main goal as it allows for an increase in quality of the measurements. Unfortunately, for the very same reasons, the high frequency vibrations have increased. As a result of this, the acoustic noise inherent in the system has worsened. An analysis of the level of streaking in measurement data was performed to ascertain whether or not the changes to the scanner has reduced this effect. Figure 3.20 shows the repeat analysis to be compared with the data from figure 3.7.

Looking at the standard deviation of the calculated centre points as before we obtain a value of 0.42 mm. This shows a reduction of 58.8 % in the pointing inaccuracies due to vibration. Despite showing an improvement, it is not of the order that was hoped when this work was undertaken. With this level of streaking it may still be necessary to have a wait period after scanner moves position to allow vibrations to be damped.

## 4 Development of Beam Alignment Technique

The purpose behind all of the previously discussed upgrades is to have a more efficient and accurate system for the characterisation of optical components. When dealing with optical systems that involve a beam propagating over a distance from transmitter to receiver the most important part of the set-up involves the alignment of the system.

As part of my project it was decided to design and implement a new alignment procedure. This new procedure would be more efficient and more robust than the methods currently in use. The basic principle of the new method involves the analysis of a preliminary low-resolution scan of the outputted beam from the optical system.

A model of the beam profile is to be fitted to the actual measurement data. From this fit we look to determine parameters like positional offset and alignment angle. Once these parameters are recorded we can either physically correct for misalignment or include it in the post-processing of the data.

This new method should prove to be a lot less tedious and time consuming to the methods currently in use. These methods are predominantly geometrical, though other approaches such as the measurement of the total transmission power have also been used.

## 4.1 Current Methods

The methods being used for alignment at the beginning of my project were quite time consuming. Most commonly geometrical methods were used to align the system and this involved many different instruments including spirit levels, laser pointers and rulers. The use of these instruments can result in accurate alignment, but since even the smallest misalignment can cause issues with coupling between transmitter and receiver a large amount of care must be taken.

Another important point to note is that as there was no specific outline to this type of alignment procedure, the accuracy is heavily dependent on the user performing it. As well as the geometrical methods, the measurements from the VNA can also be utilised for the purposes of alignment.

We expect a maximum transmission power when the transmitter and receiver are perfectly aligned. By adjusting the position and angle of orientation of the receiver with respect to the transmitter we can improve alignment by watching how the total transmission power changes. This method, much like the previous one is tedious and time consuming and does not guarantee a perfect alignment.

It was obvious at this stage that a standard alignment procedure needed to be developed. The method should be robust enough to deal with the various types of systems that are constructed on the optical bench. As well as this, the procedure should be efficient and easy to carry out.

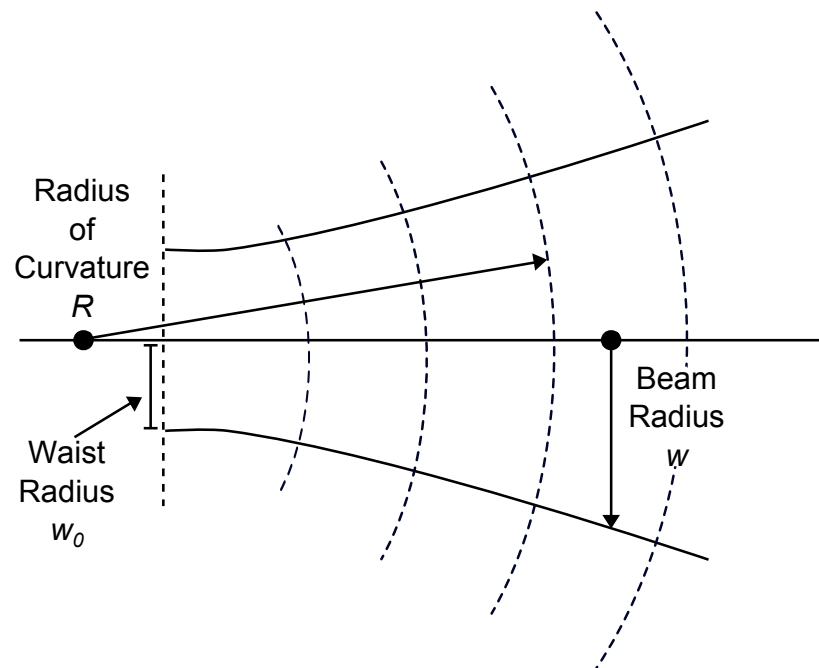


**Figure 4.1:** A schematic diagram of a beam propagating in our system. The drawing shows how the waist radius, beam radius and radius of curvature are measured.

## 4.2 New Method

It was decided that the new alignment method would be a computational process. The data from a "rough" preliminary scan would be compared to a model of what the data is expected to look like. For the majority of the measurements, with the near field scanning system, the profile of the data should be Gaussian in nature. As mentioned in Chapter 2 there are diffraction effects being caused by the comparative size of the optical components and the wavelength of the radiation. It is this diffraction that causes the beam profiles to take on a Gaussian shape.

Most of the power in the beam that is propagating through our system is concentrated at the centre. This power reduces as we move orthogonally from the axis of propagation. As the beam propagates (shown in figure 4.1) the radius ( $w$ ) increases. This increase in radius means that the power must be spread,

resulting in a larger beam and a lower peak magnitude. The evolution of the shape of the beam can be described as a fundamental Gaussian beam mode as shown in "Quasioptical Systems" [1].

In order to construct a model that can be used as a comparison with measurement data, there must be a set of defined initial parameters. Included in these are the waist radius of the beam and the radius of curvature. These values should then evolve as the propagation distance is increased. As alignment is the purpose of developing the model in the first place, there must also be parameters that define the position of the measurement plane with respect to the source. These come in the form of an orthogonal offset distance in both axes and angles that define how the measurement plane intersects the beam.

By fitting this model to the measured data, it will be possible to then determine the initial parameters associated with the measurement. This information can then be used to align the optical system correctly. As there are several different parameters to fit, some of which are dependant on each other, we need good initial guesses for our fitting routine. The approximations for each of the parameters are used in a standard non-linear fitting algorithm, in this case the Levenberg-Marquardt method. This "LM" method is used to reduce a merit function which determines the "goodness" of the fit between the model and the measurement data.

This section will detail the construction of the Gaussian beam model that was created originally in the MATLAB environment and then in LabVIEW. The transfer from MATLAB to LabVIEW was carried out in order to implement the alignment method as part of the GHOST motion control software. We will also discuss both the parameter approximations and the derivation of the Levenberg-Marquardt non-linear fitting method for complex data.

### 4.2.1 Model Construction

For the construction of our model, we need to be able to calculate the complex amplitude of the electric field of a Gaussian beam as it propagates over a distance. The nature of the evolution of the beam depends on many initial factors.

The waist radius of the beam is dependent on the size of the aperture of the transmitting antenna horn or waveguide in use. As the beam travels away from the transmitting component the beam radius evolves as shown in equation 4.1.

$$w = w_0 \left[ 1 + \left( \frac{\lambda z}{\pi w_0^2} \right)^2 \right]^{\frac{1}{2}} \quad (4.1)$$

In the above case  $w_0$ ,  $\lambda$  and  $z$  are the waist radius, wavelength and propagation distance respectively. As the beam propagates the beam radius expands due to diffraction effects at the transmitter. It is obvious that the diffraction of the beam as it leaves the aperture is going to be heavily dependent on the wavelength.

The radius of curvature ( $R$ ) defines the equiphase surface of the beam. Small values for  $R$  introduce a large phase delay in the beam relative to the centre of propagation, this idea is illustrated in fig.4.2. As the value of  $R$  approaches infinity, the characteristics of the beam approach that of a propagating plane wave. The parameter  $R$  is described by the same parameters as the beam radius and is shown in equation 4.2.

$$R = z + \frac{1}{z} \left( \frac{\pi w_0^2}{\lambda} \right)^2 \quad (4.2)$$

For the description of our beam after it has propagated a distance  $z$ , the last parameter we need to be concerned with is the phase shift of the beam. We can calculate a value for  $\phi_0$  by again using the same initial parameters as eq.4.1 and

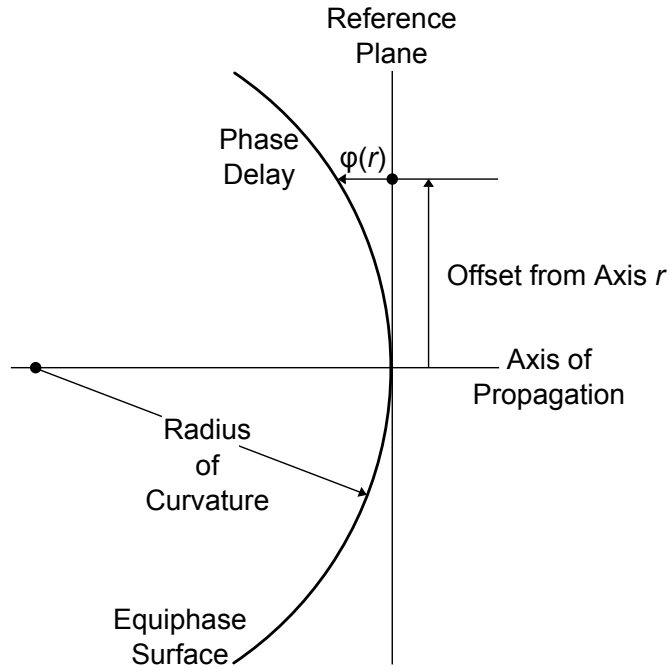


**Figure 4.2:** An illustration of how the phase front of the beam evolves as it propagates. The radius of curvature is directly related to the phase delay of the beam.

eq.4.2. Equation 4.3 shows how  $\phi_0$  is calculated at a particular point along the axis of propagation.

$$\phi_0 = \tan^{-1} \left( \frac{\lambda z}{\pi w_0^2} \right) \quad (4.3)$$

All of these parameters have been presented in a general form, however if we wish to calculate the complex amplitude of the two-dimensional surface of the beam we need to calculate these values in both the x and y axes. The electric field at any point on the propagating surface is then given by equation 4.4.

$$E(x, y, z) = \left( \frac{2}{\pi w_x w_y} \right)^{\frac{1}{2}} \cdot \exp \left[ -\frac{x^2}{w_x^2} - \frac{y^2}{w_y^2} - \frac{j\pi x^2}{\lambda R_x} - \frac{j\pi y^2}{\lambda R_y} + \frac{j\phi_{0x}}{2} + \frac{j\phi_{0y}}{2} \right] \quad (4.4)$$



This equation allows us to calculate the complex amplitude of the electric field as a function of the positional coordinates  $x$ ,  $y$  and  $z$ . In order to simplify our model it was decided that at first we would only deal with beams that were axially symmetric. For this special case many of our initial parameters are identical to each other as shown in equation 4.5.

$$w_{0x} = w_{0y} \quad (4.5a)$$

$$R_x = R_y \quad (4.5b)$$

$$\phi_{0x} = \phi_{0y} \quad (4.5c)$$

At this point we have all the tools needed to model the complex amplitude of a propagating beam at a particular point in space. In most cases our beam measurements using the near-field scanning system involve taking a planar cut through a beam at a particular propagation distance. With equation 4.4 we can mimic our measurement scan pattern and model what the expected complex amplitude of the beam should be at this plane. The complex amplitude of our model is dependent on all of the initial parameters that have been presented, however we must perform further manipulation in order to simulate an actual measured beam pattern.

Firstly, the outputted values from equation 4.4 are normalised values and must be scaled by an extra parameter  $A$ , the initial complex amplitude of our measurement. This variable  $A$  is dependent both on the initial magnitude and phase of our beam as it leaves the transmitting horn antenna. Our beam model is obviously a perfect simulation and assumes that the beam is both centred on the measurement plane and exactly perpendicular to it. While in most measure-

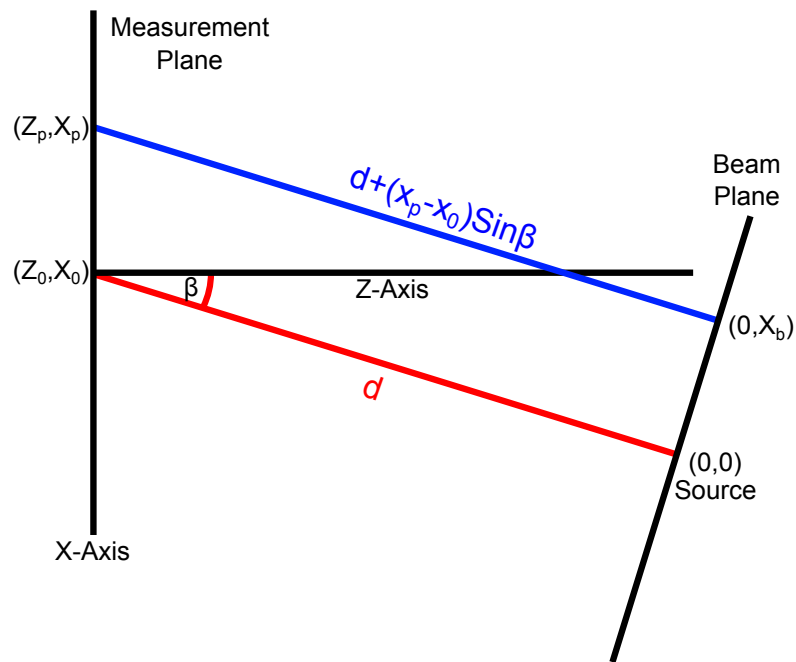


**Figure 4.3:** A two dimensional representation of the coordinate transformation performed in order to take misalignment into account.  $(z_0, x_0)$  is the point at which the measurement plane intersects the centre of the beam.

ments this would be ideal, it is almost always never the case and we must add in a layer of coordinate translation to determine the misalignment of the beam.

As we are dealing with a two-dimensional grid of data points, the coordinate translation for the Gaussian model must involve the re-mapping of our three positional coordinates  $x$ ,  $y$  and  $z$ . However, for the sake of simplicity the translation shall first be introduced for just two of these coordinates  $x$  and  $z$ . Figure 4.3 shows a representation of two planes that are misaligned.

When making a measurement with the scanning system or generating a model, the coordinates that represent the scan grid are given in the measurement plane reference frame. The calculation of  $E(x, y, z)$  for the Gaussian beam model needs its inputted coordinates to be in the frame of reference of the beam plane. Therefore, the measurement plane coordinates must be translated into the frame of

reference of the beam to calculate the correct complex amplitudes.

In this example the centre of the beam intersects the measurement plane at the coordinates  $(z_0, x_0)$  in the measurement plane which is the equivalent of  $(d, 0)$  in the beam plane's reference frame. To simplify further we can arbitrarily set the value of  $z_0$  to be 0. All other coordinates along the measurement plane can be then translated by calculating with respect to the angle  $\beta$  as in equations 4.6 and 4.7.

$$z_b = d + (x_p - x_0) \sin \beta \quad (4.6)$$

$$x_b = (x_p - x_0) \cos \beta \quad (4.7)$$

Expanding the translation to deal with a two dimensional plane involves performing the exact same type of translation on the y-axis. This gives rise to the addition of four new initial parameters for the Gaussian beam model.  $x_0$  and  $y_0$  define the point at which the beam will intersect the measurement plane.  $\alpha$  and  $\beta$  define the angle that the axis of propagation intersects the vertical and horizontal measurement plane axes respectively.

$$\begin{bmatrix} \cos \alpha & 0 & -\sin \alpha \\ 0 & \cos \beta & -\sin \beta \\ -\sin \alpha & -\sin \beta & -\cos \alpha - \cos \beta \end{bmatrix} \begin{bmatrix} x_p \\ y_p \\ z_p \end{bmatrix} + \begin{bmatrix} -x_0 \cos \alpha \\ -y_0 \cos \beta \\ x_0 \sin \alpha + y_0 \sin \beta + d \end{bmatrix} = \begin{bmatrix} x_b \\ y_b \\ z_b \end{bmatrix} \quad (4.8)$$

Equation 4.8 shows the transformation matrix that is used to convert our measurement plane coordinates. With the simplification of ensuring the beam is axially symmetric, the need to take into account a third angular misalignment is eliminated. This third angle if used, would define the "roll" of the beam.

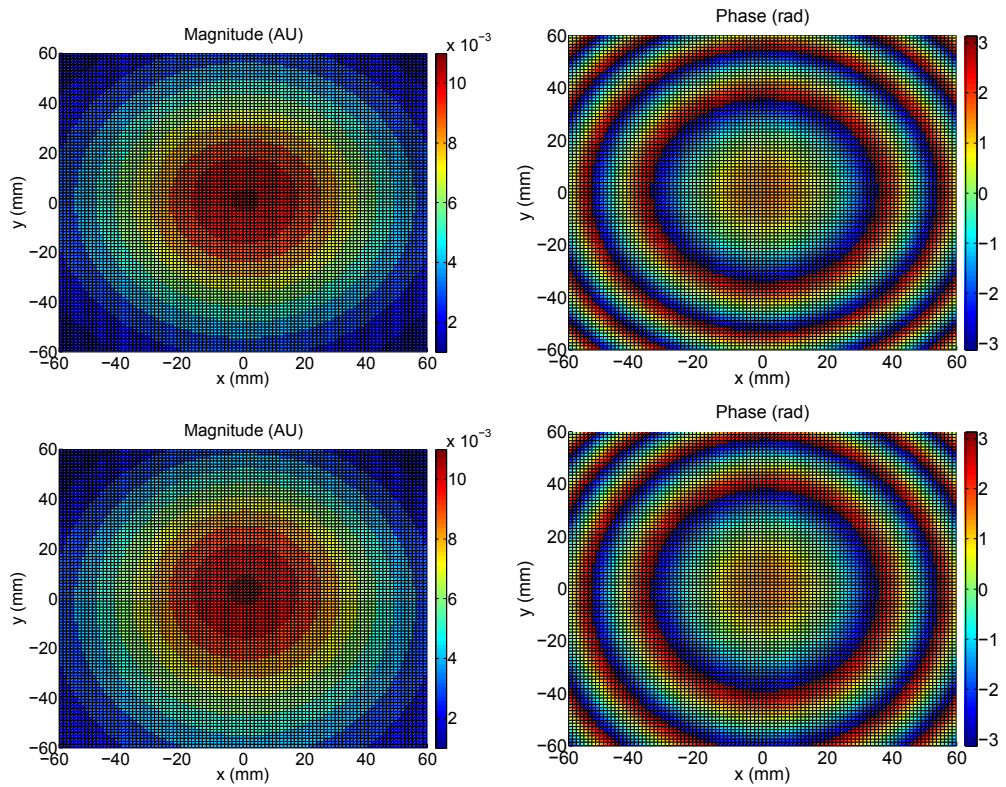


**Figure 4.4:** A comparison between the beam model with and without a tilt angle. The top row shows a planar cut through a beam with no misalignment and the bottom row shows a beam at a 25 degree tilt angle in the horizontal axis

## 4.2.2 Gaussian Beam Model Summary

In order to create the Gaussian beam model we need the wavelength ( $\lambda$ ) of the radiation, eight initial parameters and a set of coordinates that defines the measurement plane. The waist radius of the beam  $w_0$  is dependent on the size of the aperture of the source. This parameter along with the propagation distance  $z$  is used to calculate the beam radius  $w$ .

The parameters  $x_0$  and  $\beta$  are used to describe the alignment of the source with the horizontal axis of the measurement plane. Positive values for the angle  $\beta$  represent a tilting of the source to the right. As the measurement plane faces

the source this causes the point of intersection of the beam centre to travel to the left. This convention is also used for the vertical axis with the parameters  $y_0$  and  $\alpha$ .

The last two parameters that are inputted into the model are the initial magnitude and phase of the beam. These values are used to calculate the complex amplitude  $A$  which is used as a scaling factor for the model.

### 4.2.3 Complex Levenberg-Marquardt Implementation

There are many standard methods used for the fitting of models to measurement data. For the purpose of fitting the Gaussian beam model to actual measurements a non-linear fitting method is used. The Levenberg-Marquardt (LM) method was selected for use in this case. This method is commonly used and an algorithm can be found in any version of Numerical Recipes [23]. Unfortunately the implementation that is described is designed for dealing with real valued data and our measurement data is complex. As a result of this the LM method needs to be modified in order to deal with complex data.

All fitting methods involve the reduction of a merit function that determines how close a model compares with a collection of data. This  $\chi^2$  merit function is shown in its general form in equation 4.9. The difference between each point on the model with its corresponding point of data is weighted by a value  $\sigma$  and are then summed together. The lower the resulting value of  $\chi^2$ , the closer or model agrees with the data. Equation 4.10 shows how our merit function is altered to account for complex values.

$$\chi^2(\mathbf{a}) = \sum_{i=1}^N \left[ \frac{y_i - y(x_i; \mathbf{a})}{\sigma_i} \right]^2 \quad (4.9)$$

$$\chi^2(\mathbf{a}) = \sum_{i=1}^N \left[ \frac{(y_i - y(x_i; \mathbf{a}))^* (y_i - y(x_i; \mathbf{a}))}{\sigma_i^2} \right] \quad (4.10)$$

The LM fitting method varies between two different methods for reducing the merit function. The variation is dependant on how far the fitted data is away from the correct solution. The steepest descent method is utilised when the fit is far from the solution and as a minimum is approached the LM method uses an inverse-Hessian method.

To implement the LM routine two pieces of mathematical scaffolding must first be set up. Both the Hessian matrix  $\alpha_{kl}$  and gradient vector  $\beta_k$  need to be calculated. The size of these two structures is dependent on the amount of parameters that are used to create the model. Equations 4.11 and 4.12 show how both are calculated.

$$\alpha_{kl} = \frac{1}{2} \frac{\partial^2 \chi^2}{\partial a_k \partial a_l} \quad (4.11)$$

$$\beta_k = -\frac{1}{2} \frac{\partial \chi^2}{\partial a_k} \quad (4.12)$$

For the construction of equation 4.12, it is necessary to perform a first order partial derivative of equation 4.10 with respect to each parameter. This process is outlined in equations 4.13 and 4.14.

$$\frac{\partial \chi^2(\mathbf{a})}{\partial a_k} = \sum_{i=1}^N \frac{1}{\sigma_i^2} \left[ (y_i - y(x_i; \mathbf{a})) \left( \frac{-\partial y(x_i; \mathbf{a})^*}{\partial a_k} \right) + (y_i - y(x_i; \mathbf{a}))^* \left( \frac{-\partial y(x_i; \mathbf{a})}{\partial a_k} \right) \right] \quad (4.13)$$

$$\frac{\partial \chi^2(\mathbf{a})}{\partial a_k} = -2 \sum_{i=1}^N \frac{1}{\sigma_i^2} \text{RE} \left[ (y_i - y(x_i; \mathbf{a})) \left( \frac{-\partial y(x_i; \mathbf{a})}{\partial a_k} \right) \right] \quad (4.14)$$

For the Hessian matrix the partial derivatives of the combinations of all parameters must be carried out and this is outlined in equation 4.15.

$$\frac{\partial^2 \chi^2(\mathbf{a})}{\partial a_k \partial a_l} = -2 \sum_{i=1}^N \frac{1}{\sigma_i^2} \text{RE} \left[ \left( \frac{\partial y(x_i; \mathbf{a})}{\partial a_k} \right) \left( \frac{-\partial y(x_i; \mathbf{a})}{\partial a_l} \right) + (y_i - y(x_i; \mathbf{a})) \left( \frac{\partial^2 y(x_i; \mathbf{a})}{\partial a_k \partial a_l} \right) \right] \quad (4.15)$$

It should be noted that the value of  $\frac{\partial^2 \chi^2(\mathbf{a})}{\partial a_k \partial a_l}$  depends on both the first and second order derivatives of the basis functions with respect to their parameters. For a successful fit the sum over all values of  $i$  tends to cancel out the second order derivative. According to the literature, including this term does not help the fitting method and in some cases can actually be destabilising [23]. For this implementation, as is the general case, this term will be ignored as in equation 4.16.

$$\frac{\partial^2 \chi^2(\mathbf{a})}{\partial a_k \partial a_l} = 2 \sum_{i=1}^N \frac{1}{\sigma_i^2} \text{RE} \left[ \left( \frac{\partial y(x_i; \mathbf{a})}{\partial a_k} \right) \left( \frac{\partial y(x_i; \mathbf{a})}{\partial a_l} \right) \right] \quad (4.16)$$

Now that the partial derivatives have been evaluated, both the gradient vector and the Hessian matrix can be rewritten in the form shown in equations 4.17 and 4.18.

$$\alpha_{kl} = \sum_{i=1}^N \frac{1}{\sigma_i^2} \text{RE} \left[ \left( \frac{\partial y(x_i; \mathbf{a})}{\partial a_k} \right) \left( \frac{\partial y(x_i; \mathbf{a})}{\partial a_l} \right) \right] \quad (4.17)$$

$$\beta_k = \sum_{i=1}^N \frac{1}{\sigma_i^2} \text{RE} \left[ (y_i - y(x_i; \mathbf{a})) \left( \frac{-\partial y(x_i; \mathbf{a})}{\partial a_k} \right) \right] \quad (4.18)$$

One more adjustment needs to be performed in order to ready the Hessian matrix for use in the LM method. As mentioned previously this routine involves switching between two different methods of reducing the merit function and

this is hard-coded into the Hessian matrix. All of the diagonal elements are manipulated as in equation 4.19, where  $\lambda$  is a non-dimensional fudge factor that determines whether or not the matrix will be diagonally dominant [23].

$$\alpha'_{jj} = \alpha_{jj}(1 + \lambda) \quad (4.19)$$

The fitting algorithm itself is very straight forward and just involves solving the set of linear equations shown in equation 4.20. After adjusting each of the parameters with its corresponding value for  $\delta a$  the merit function is re-evaluated. If  $\chi^2$  has been reduced then the fudge factor is decreased and the linear equations are solved once again. Otherwise we increase the fudge factor before attempting to solve 4.20 again.

$$\sum_{i=1}^M \alpha'_{kl} \delta a_l = \beta_k \quad (4.20)$$

The LM routine has multiple stopping criteria in order to prevent it from iterating infinitely. The two main exiting conditions are limits on the maximum size of the fudge factor and a maximum number of iterations.

#### 4.2.4 Initial Guesses for LM Fitting

In initial tests of the fitting algorithm, the results were seen to be unreliable. These tests actually involved fitting the model to simulated data which used the same model with random initial parameters. With this we were able to compare the fitted initial parameters with the parameters that were used to generate the data. A large proportion of the tests resulted in the fitting routine falling into a minimum that was not the correct solution.



It is believed that the sheer number of parameters and the fact that some of them were interdependent was causing problems for the algorithm. These problems disappeared when initial guesses that were relatively close to the values for the parameters were used. A method of determining reasonable estimates for some of the fitting parameters before running the Levenberg-Marquardt algorithm was needed. These approximations would need to come directly from the data that we are attempting to fit to.

Initially a determination of the approximate location of the centre of the beam was needed. Searching for a maximum value for magnitude would not be a reliable way to do this. Not only is there a risk of identifying a false centre due to noise issues in actual measurements, but a method like this would also be very restrictive. For ideal data searching in this manner would only allow us to determine the point on the measurement that is closest to the centre. In cases where we are taking low resolution scans this could lead us to find a centre point that is more than a millimetre from the true centre.

In order to determine the true centre of our beam at the measurement plane, we determine the centroid of the beam. This process is shown in equation 4.21, where  $I$  is the value of the magnitude at each point and is used to weight the coordinates. As is shown this calculation must be carried out twice to determine both the  $x$  and  $y$  coordinates of the central point. From this we can obtain the geometrical centre of the beam even if it lies on a point that was not actually measured.

$$x_{centre} = \frac{\sum_{i=1}^N I(x_i, y_i) \cdot x_i}{\sum_{i=1}^N I(x_i, y_i)} \quad (4.21a)$$

$$y_{centre} = \frac{\sum_{i=1}^N I(x_i, y_i) \cdot y_i}{\sum_{i=1}^N I(x_i, y_i)} \quad (4.21b)$$

Now that an approximate value for the centre point of the beam at the measurement plane has been acquired, it can be used to approximate the beam radius. The  $D4\sigma$  definition of the beam radius allows us to do this with ease. This ISO standard states that the diameter of the beam is four times the value of the standard deviation of the beam, with the radius being half of this value. Since the beam is circularly symmetric we can approximate  $w$  from equation 4.22, where  $x_0$  and  $y_0$  are the centre points from equation 4.21. The factor of two that the standard deviation should be multiplied by is not present as it cancels when we attempt to find an average of the waist calculated in both axes. Equation 4.22 has been tested on simulated data to ensure consistency.

$$w = \sqrt{\frac{\sum_{i=1}^N I(x_i, y_i)(x - x_0)^2 + \sum_{i=1}^N I(x_i, y_i)(y - y_0)^2}{\sum_{i=1}^N I(x_i, y_i)}} \quad (4.22)$$

This value of the beam radius that has been calculated must be used in conjunction with a value for the radius of curvature in order to determine the waist. Unfortunately, approximating a value for  $R$  is not as straightforward as the centre or beam radius. The phase information contained in the complex amplitude must be used in order to estimate  $R$ .

As was shown previously in figure 4.2 the radius of curvature of the beam is directly related to the phase delay. This phase delay which is measured in radians can be converted to an actual geometrical delay when the wavelength of the propagating radiation is taken into account. The conversion can be seen in equation 4.23, where  $z_{lag}$  is the geometrical distance that the equiphase surface is from the measurement plane. When used in conjunction with the  $x$  and  $y$  coordinates we can now describe positions on this surface in three dimensional space.

$$z_{lag} = \frac{\phi\lambda}{2\pi} \quad (4.23)$$

The phase data, now showing the phase front geometrically, can be approximated as a section of a sphere. If the function that describes this sphere can be determined a value for the radius of curvature can be ascertained. There is however an obstacle that must be dealt with before a sphere can be fitted, the phase data must be unwrapped.

The values that describe the phase of the beam are wrapped from  $-\pi$  to  $\pi$ . Unwrapping a two dimensional grid of phase data is non-trivial, especially in this case where the coordinate grid is Cartesian in nature. The simplest solution to this problem is to take two cuts through the data, one vertical and one horizontal. These cuts should intersect at the central point of the measurement data. As the central point that has been calculated most likely does not lie on the coordinate grid for the data, the slices must be interpolated from the phase data. When phase slices are being interpolated it is useful to also store the corresponding values of magnitude for the purpose of weighting the phase data. The closer we are to the centre of the beam, the closer the shape our phase is to a sphere and for this reason should be weighted heavier for fitting purposes.

To perform the actual unwrapping on our newly acquired phase slices, we must start at the centre point. The centre will have the maximum value of phase and the data needs to be unwrapped with respect to this. The simplest way to do this is to split each of the slices at the centre and unwrap each section separately before stitching them back together. At this point we should have two slices that represent the geometrical coordinates of the equiphase surface.

The model of the sphere (eq.4.24 and eq.4.25) that we are using to determine the radius of curvature has four parameters. These need to be adjusted in order to

minimise the merit function. It was thought that these parameters  $R$ ,  $x_0$ ,  $y_0$  and  $z_0$  also had the potential to give us estimates for more than just  $R$ .

$$R = \sqrt{(x - x_0)^2 + (y - y_0)^2 + (z - z_0)^2} \quad (4.24)$$

$$z = \sqrt{R^2 - (x - x_0)^2 - (y - y_0)^2} + z_0 \quad (4.25)$$

The fitted sphere gives us a value for the its centre as well as its radius of curvature. The position of the centre of our sphere should be analogous to the position of the source of our beam. By comparing these coordinates with the location of the centre of the beam at our measurement plane, an initial guess for the angles of misalignment was thought to be possible. Unfortunately all attempts to use the location of the sphere centre to determine directional information failed. As the sphere that is defined by our phase is generally very large, the data points that we have from our phase slices only encapsulate a very small section of its surface. Due to this, determining the position of the centre of the sphere to any meaningful accuracy is not possible. Despite this, the method works very well for estimating a value for  $R$ .

With estimates for both  $R$  and  $w$  along with a known value for the wavelength, it is now possible to calculate approximate values for two of the initial parameters needed for the model. These quantities are  $w_0$  and  $z$  which are found using equations 4.26 and 4.27 respectively.

$$w_0 = \sqrt{\frac{\lambda^2 R^2}{\pi^2 w^2 + \frac{\lambda^2 R^2}{w^2}}} \quad (4.26)$$

$$z = \frac{R + \sqrt{R^2 - \frac{4\pi w_0^4}{\lambda^2}}}{2} \quad (4.27)$$

At this point there are now very good estimates for half of the initial parameters of the model. With these estimates the fitting algorithm becomes a lot more stable and is ready to be fully tested.

#### 4.2.5 Testing the Fitting Method

For the first testing stage of the fitting method we need a controlled environment. To achieve this actual measurement data is not used. Instead, measurement data is simulated and the model is then fitted. This allows for the study of how close the fitted parameters are to the values that they should be.

Using simulated data that contains no noise, the fitting algorithm gives us perfectly correct data in almost all cases. The situations where this breaks down generally occur for either very large and unrealistic misalignment angles or in cases where our simulated data does not encompass enough of the beam (figure 4.5).

At the very least it must be ensured that a measurement scan will encompass twice the beam radius if it is to be used for alignment purposes. If the scan area is too small our estimates of the initial parameters fail and the fitting algorithm becomes very unreliable.

Showing that the algorithm works for perfect simulated data only proves that the complex fitting algorithm works. It does not show if it is viable for use with real measurement data. In order to make the simulated data more realistic a layer of random noise should be added to the values. Noise must be added separately to

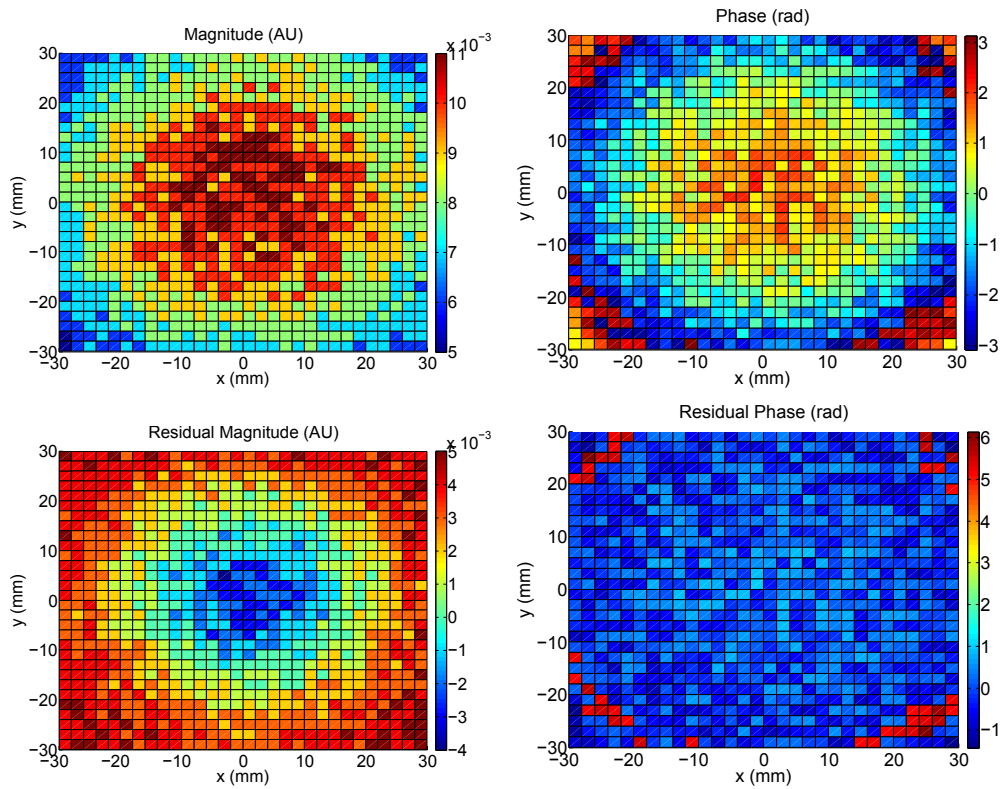


**Figure 4.5:** Data from a failed attempt to fit the Gaussian model. The top row shows the magnitude and phase of the simulated data. Under this are the residuals between the simulated data and the fitted model.

the magnitude and phase of the beam. The noise that we add to the magnitude is weighted to the value of the magnitude at each point. This allows for more realistic values at the extremities of the beam. With regard to the phase the simulated noise is allowed to be completely random but is limited to a range of  $[-\frac{\pi}{4}, \frac{\pi}{4}]$  in order to avoid problems with phase wrapping. Figure 4.6 shows what the model looks like with noise scaled to 10 % of the magnitude added to it.

Now that the simulating measurement data is more realistic, it can be used to reliably test the fitting algorithm. Testing in this way should prove if this method is viable to use as an alignment tool. Multiple tests were run for different levels of noise. As the level of noise increases, the quality of the solution obtained by

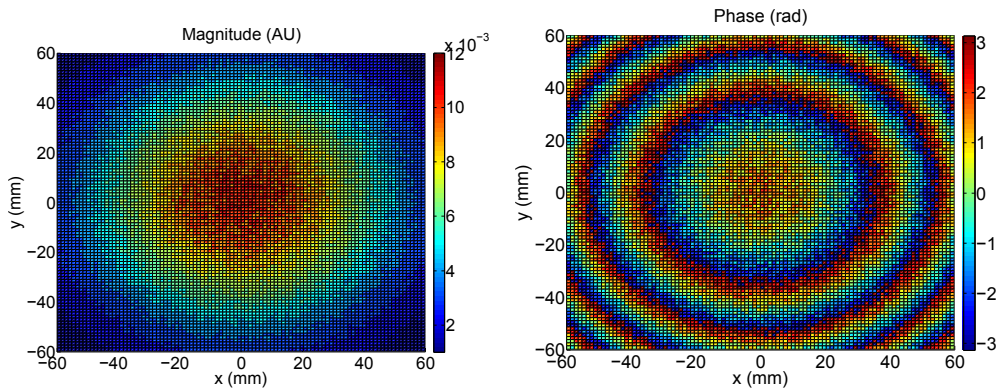


**Figure 4.6:** The Gaussian model with noise added to it. This particular case has random noise scaled to 10% of the magnitude added to each value of magnitude and random noise in the range of  $[-\frac{\pi}{4}, \frac{\pi}{4}]$  added to the phase.

fitting deteriorates. If more of the beam is captured and the resolution of the simulated data is increased a higher level of noise can be dealt with but there is little point to this. It would not be useful to have to perform a very detailed scan for the purpose of alignment as this would decrease the overall efficiency of measurements.

As there is a trade-off between the size and resolution of the scan with the amount of noise in the data, it would be ideal to determine what level of noise can be dealt with for low resolution scans. Figure 4.7 shows an example of a simulated data test. The virtual scan is low resolution (31 x 31 points) and would take less than 15 minutes to actually carry out with the new motion control system.

In this particular case the model has converged to a solution that is very close to the simulated data. The residuals for magnitude are for the most part a factor of 10 smaller than the actual magnitude values. However, it is the phase that is the most important when it comes to determining directional information and the residuals are very small here. Table 4.1 shows how well the fitted

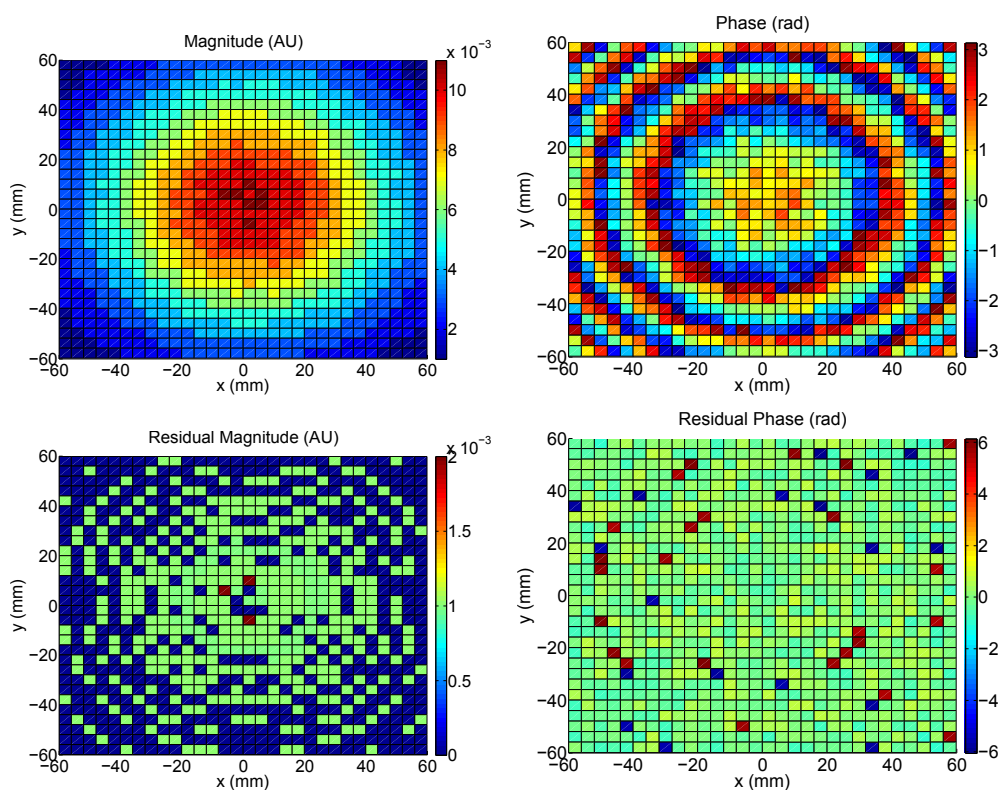


**Figure 4.7:** Shown here are plots of the magnitude and phase of the simulated data used for a test along with the residuals with respect to the fitted model. This simulated scan is low resolution (31 x 31 points) over an area of 120 mm<sup>2</sup>.

parameters agree with those that were used to generate the simulated data. For this simulation the noise was weighted to 4 % of the magnitude value at each point.

#### 4.2.6 Fitting Measurement Data

We now know that the algorithm is capable of determining the initial parameters of simulated noisy data to a high degree of accuracy. With the information that has been garnered from simulation it is now time to show that the fitting routine can be used with real measurement data.



	<b>Initial Parameters (Sim. Data)</b>	<b>Fitted Parameters</b>
$w_0$	8.741 mm	8.696 mm
$Z$	781.77 mm	781.03 mm
$\alpha$	-12.18°	-12.09°
$\beta$	-11.45°	-11.39°
$x_0$	-0.39 mm	-0.38 mm
$y_0$	-0.95 mm	-0.89 mm

**Table 4.1:** A comparison between the initial parameters of the simulated data and the fitted parameters.

As the fitting method will be used as part of an alignment procedure, it is necessary to restrict the measurement grid size for the sake of efficiency. In the measurement that will be used to test the routine a step size of 4 mm in a grid of 31 x 31 points (120 mm<sup>2</sup>) is chosen.

The optical system that is set-up for the purpose of testing consists of two identical corrugated antenna horns. The antenna horns are separated by 170 mm and roughly aligned. The scan was performed with no delay between measurement steps in order to ascertain whether any streaking present in the system would have an adverse effect on the alignment procedure.

With the new motion control system this preliminary alignment scan took 10 minutes to perform. Once complete the data was inputted into the fitting routine and figure 4.8 shows the measurement and residuals. As was the case with fitting to the noisy simulated data, the magnitude residuals are a factor of 10 less than the magnitude values and the phase data agrees even better than this.

The last stage to the testing of this alignment tool is to determine how accurately the alignment parameters themselves are being determined. To do this, the measurement from figure 4.8 is carried out again. However, this time we adjust

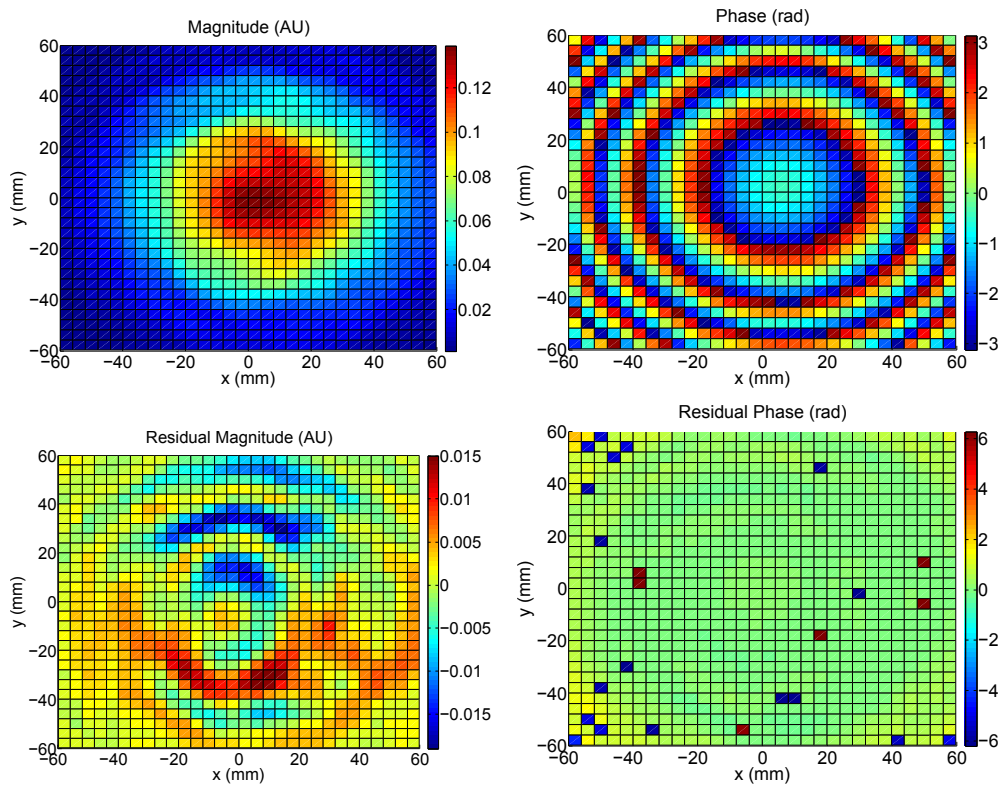


**Figure 4.8:** Measurement values and residuals for both magnitude and phase.

This scan is a low resolution ( $31 \times 31$ ) scan over an area of  $120 \text{ mm}^2$ .

the centre of our scan to be  $-20 \text{ mm}$  offset in both the horizontal and vertical axes. What is expected here is to obtain the exact same fitted parameters as before except for the values of  $x_0$  and  $y_0$ . These two parameters should both have decreased by  $20 \text{ mm}$ .

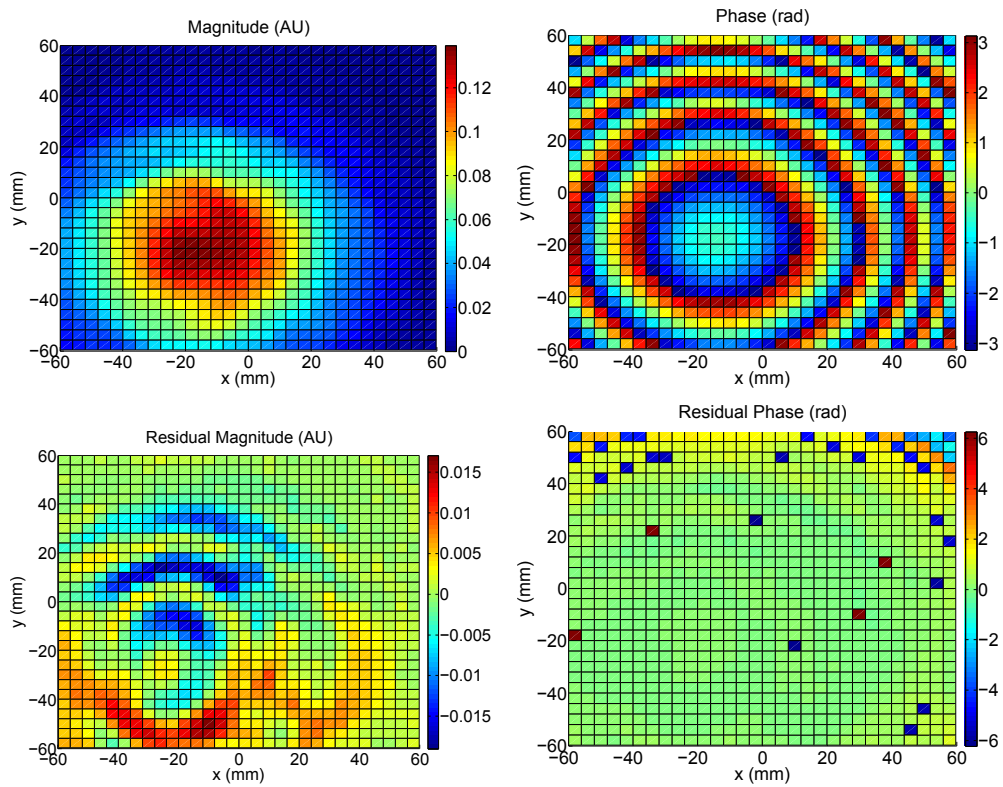


**Figure 4.9:** A repeat of the measurement from figure 4.8 with the centre point offset by  $-20$  mm in both the horizontal and vertical axes.

Table 4.2 shows the fitted parameters for the measurements from figure 4.8 and figure 4.9. With the horn to horn distance being set at 170 mm we can see that the fitted parameters give us a very good estimate of the propagation distance. The calculated waist radius of the horn being used for transmission is 5.2 mm and again our fitted parameters give us a good estimate of this.

The changes in the  $x_0$  and  $y_0$  parameters are  $-20.05$  mm and  $-19.99$  mm respectively. These values agree very closely with offset distances that were set for the second measurement with respect to the first. The only worrying result from this test is the change in the alignment angles  $\alpha$  and  $\beta$ . For this test, these values should not have changed and this may suggest a possible problem with the alignment tool.

	<b>Fitted Parameters Fig.4.8</b>	<b>Fitted Parameters Fig.4.9</b>
$w_0$	5.85 mm	5.86 mm
$z$	171.4 mm	170.9 mm
$\alpha$	$-0.74^\circ$	$-3.08^\circ$
$\beta$	$-0.24^\circ$	$-1.81^\circ$
$x_0$	4.24 mm	$-15.81$ mm
$y_0$	0.47 mm	$-19.52$ mm

**Table 4.2:** The fitted parameters for two measurements using the near field scanner. Note that the propagation distance  $z$  has been found to be almost identical to the horn to horn distance of the optical set-up.

## 5 Conclusions

The purpose of this project was to optimise the near field scanning system that is in use in the Experimental Physics Department at NUI Maynooth. The system is used in conjunction with a ZVA-24 Vector Network Analyser for the characterisation and verification of optical components in the mm and sub-mm range. This thesis has outlined the purpose behind the measurements made using the scanning system along with the principle of operation of the VNA. The original set up of the scanner was also discussed as well as the flaws in its implementation. Any upgrades to the system and subsequent problems were outlined and a new tool for use in the alignment of optical systems was proposed.

The biggest issue with the scanning system was its efficiency. This was quite poor due to the slow maximum speed at which it was able to move. When compared with the power of its driving motors the scanner could be seen to be heavily under-performing. In order to increase the speed at which the scanner was able to move from point to point an entirely new motion control system was designed and developed.

The newly designed system provided a dramatic increase in the maximum velocity of the scanner; from 300 steps/s to 8500 steps/s. Other upgrades were also carried out to allow for better tracking of the motion of the scanner. New translation stages were added to the system to allow for more degrees of freedom

when testing an optical system. With the extra translation stages there was added danger to the user and new safety features for the system were also developed.

As a result of the increased driving power of the actuator system, an increase in the mechanical vibrations was seen. These excitations were analysed using two different methods and their levels were monitored while the system was adjusted. The reconfiguring of the mounting of the scanner system and the adjustment of the motion control parameters were just two of the processes that were carried out in order to achieve improvement. An analysis of the streaking effect that was being caused by the increased vibrations of the scanner was the main method used in determining whether there was improvement. The results from Chapter 3 show that a decrease in the amount of streaking was achieved, however this decrease was not on the scale that was hoped for.

As a further part to the optimisation of the scanning system, a new tool for use in the alignment of the system was also developed. This tool allows us to see how well an optical system is aligned by performing a preliminary low resolution scan. The new alignment method involved the development of a Gaussian beam model that is used in conjunction with a fitting algorithm to determine the initial parameters of a measured Gaussian beam.

The new alignment tool was tested with both simulated data and real measurement data. In Chapter 4, the construction of the tool is discussed. Here we also present the step by step testing of the method and show an example of how we determine the misalignment of a simple optical system involving two antenna horns. The alignment tool is shown to be successful, but there is still room for improvement in order for it to be implemented alongside the motion control software.

Overall, the efficiency of the near field scanning system has been dramatically improved. Despite the advent of some new issues with mechanical vibrations, the speed at which a measurement can be performed has been significantly increased. The creation of a tool to be used for alignment will hopefully help solidify a standard method for alignment. With a standard method in place, we should be able to have more confidence in the reliability of future measurements using the scanning system.

### 5.0.7 Possible Future Work

As mentioned, there is still room for improvement with regards to the mechanical vibrations in the scanning system. Further reductions may be possible with additional changes to the structure. It has been suggested that the vertical shaft on which the dynamic head is mounted should be replaced with a new shaft that is not cylindrical in shape. A triangular shaft would be less sensitive to resonances in the system.

The vertical axis is still causing a large amount of acoustic noise when in motion, a detailed acoustic analysis of the system might prove to be useful. Unfortunately it seems that any decrease achieved in the acoustic noise causes an increase in the low-frequency vibrations of the scanner.

Before the alignment method can be implemented alongside the Ghost 2 motion control software, further tests must be performed. The fitting of the angles  $\alpha$  and  $\beta$  seems to be the most unreliable part of the alignment tool. Determination of the accuracy at which these angles are being calculated should be the number one priority of any future work on this alignment tool.

# Bibliography

- [1] P. Goldsmith, *Quasioptical Systems*. IEEE Press, 1998.
- [2] Planck Collaboration, “The Scientific Programme of Planck (Bluebook),” *ESA*, 2005.
- [3] A. Penzias and R. Wilson, “A Measurement of Excess Antenna Temperature at 4080 Mc/s,” *A&A*, 1965.
- [4] NASA: WMAP Science Team, “Timeline of the Universe,” released to public domain and available at <http://map.gsfc.nasa.gov/media/060915/index.html>.
- [5] W. Carrol and D. Ostlie, *An Introduction to Modern Astrophysics*,. Pearson Education, Inc., 2007.
- [6] C. Bennet, “4-Year COBE DMR Cosmic Microwave Background Observations: Maps and Basic Results,” *The Astrophysical Journal*, 1996.
- [7] N. Jarosik, “Seven-Year Wilkinson Microwave Anisotropy Probe (WMAP) Observations: Sky Maps, Systematic Errors, and Basic Results,” *The Astrophysical Journal*, 2010.
- [8] QUaD Collaboration, “First Season QUaD CMB Temperature and Polarization Power Spectra,” *The Astrophysical Journal*, 2008.



- [9] ESA: LFI & HFI Consortia, "Planck Unveils the Universe: Now and Then," released to public domain and available at <http://www.esa.int/esaMI/Planck/SEMF2FRZ5BG1.html>.
- [10] ALMA Consortium, "Timeline of the Universe," released to public domain and available at <http://www.almaobservatory.org/>.
- [11] K. Lo and A. Russel, "The Atacama Large Millimeter/Submillimeter Array Development Program," *Astro2010 Conference*, 2010.
- [12] D. Arnone, C. Ciesla, A. Corchia, S. Egusa, and M. Pepper, "Applications of Terahertz (THz) Technology to Medical Imaging," *SPIE Vol. 3828*, 1999.
- [13] L. Young, *Terahertz Imaging Systems with Medical Applications*. MSc Thesis, NUI Maynooth, 2007.
- [14] H. Mantsch and D. Naumann, "Terahertz Spectroscopy: The Renaissance of Far Infrared Spectroscopy," *Journal of Molecular Structure*, 2010.
- [15] *T8000 Datasheet*, Thruvision, 2011.
- [16] M. King, W. Buchanan, and T. Korte, "Identification and Quantification of Polymorphism in the Pharmaceutical Compound Diclofenac Acid by Terahertz Spectroscopy and Solid-State Density Functional Theory," *Journal of Analytical Chemistry*, 2010.
- [17] P. Taday, "Pharmacy Projects," in *NTTI Paris*, 2009.
- [18] R. Mavaddat, *Network Scattering Parameters*. World Scientific Publishing Company, Incorporated, January 1996, vol. 2.
- [19] B. Shincke and J. Lunn, *Basics of Vector Network Analysis*. Rohde and Schwarz, UK, 2005.

- [20] J. Lunn, *Rohde and Schwarz Millimeter Wave Vector Network Analyser Solution*. Rohde and Schwarz UK, 2007.
- [21] S. Kehoe, *An Investigation of Efficient Submillimetre Analytical Techniques & Methods of Modelling Multiple Reflections*. MSc Thesis, NUI Maynooth, 2008.
- [22] *LIS3L02AS4 Datasheet*, STMicroelectronics, 2004.
- [23] W. Press, B. Flannery, S. Teukolsky, and W. Vetterling, *Numerical Recipes in Pascal*. Press Syndicate of the University of Cambridge, 1986.